

M giants with IGRINS

I. Stellar parameters and α -abundance trends of the solar neighborhood population*

G. Nandakumar¹, N. Ryde¹, L. Casagrande^{2,3}, and G. Mace⁴

- ¹ Lund Observatory, Division of Astrophysics, Department of Physics, Lund University, Box 43, 221 00 Lund, Sweden e-mail: govind.nandakumar@fysik.lu.se; govind.iist@gmail.com
- Research School of Astronomy and Astrophysics, The Australian National University, Bart Bok Rd, Stromlo, ACT 2611, Australia

³ ARC Centre of Excellence for All Sky Astrophysics in 3 Dimensions (ASTRO 3D), Australia

Received 14 February 2023 / Accepted 28 April 2023

ABSTRACT

Context. Cool stars, such as M giants, can only be analyzed in the near-infrared (NIR) regime due to the ubiquitous titanium oxide features in optical spectra of stars with $T_{\rm eff} < 4000\,\rm K$. In dust-obscured regions, the inner bulge and Galactic center region, the intrinsically bright M giants observed in the NIR are an optimal option for studying stellar abundances and the chemical evolution of stellar populations. Because of the uncertainties in photometric methods, a method for determining the stellar parameters for M giants from the NIR spectra themselves is needed.

Aims. We develop a method for determining the stellar parameters for M giants from the NIR spectra. We validate the method by deriving the stellar parameters for nearby well-studied M giants with spectra from the spectral library of the Immersion GRating INfrared Spectrograph (IGRINS). We demonstrate the accuracy and precision of our method by determining the stellar parameters and α -element trends versus metallicity for solar neighborhood M giants.

Methods. We carried out new observations of 44 M giant stars with IGRINS mounted on the Gemini South telescope. We also obtained the full H and K band IGRINS spectra of six nearby well-studied M giants at a spectral resolving power of $R=45\,000$ from the IGRINS spectral library. We used the tool called spectroscopy made easy in combination with one-dimensional (1D) model atmospheres in a radiative and convective scheme (MARCS) stellar atmosphere models to model the synthetic spectrum that fits the observed spectrum best.

Results. The effective temperatures that we derive from our new method (tested for $3400 \lesssim T_{\rm eff} \lesssim 4000$ K here) agree excellently with those of the six nearby well-studied M giants, which indicates that the accuracy is indeed high. For the 43 solar neighborhood M giants, our $T_{\rm eff}$, $\log g$, [Fe/H], $\xi_{\rm micro}$, [C/Fe], [N/Fe], and [O/Fe] agree with APOGEE with mean differences and a scatter (our method – APOGEE) of -67 ± 33 K, -0.31 ± 0.15 dex, 0.02 ± 0.05 dex, 0.22 ± 0.13 km s⁻¹, -0.05 ± 0.06 dex, 0.06 ± 0.06 dex, and 0.02 ± 0.09 dex, respectively. Furthermore, the tight offset with a small dispersion compared to the APOGEE $T_{\rm eff}$ indicates a high precision in our derived temperatures and those derived from the APOGEE pipeline. The typical uncertainties in the stellar parameters are found to be ±100 K in $T_{\rm eff}$, ±0.2 dex in $\log g$, ±0.1 dex in [Fe/H], and ±0.1 km s⁻¹ in $\xi_{\rm micro}$. The α-element trends versus metallicity for Mg, Si, Ca, and Ti are consistent with the APOGEE DR17 trends for the same stars and with the GILD optical trends. We also find a clear enhancement in the abundances for thick-disk stars.

Key words. stars: fundamental parameters – stars: abundances – stars: late-type – techniques: spectroscopic – Galaxy: abundances

1. Introduction

As necessary ingredients in any spectroscopic analyses, and specifically, in order to accurately estimate detailed elemental abundances from stellar spectra, it is crucial to determine the fundamental stellar parameters. These are the effective temperature ($T_{\rm eff}$), surface gravity ($\log g$), metallicity ([Fe/H]), and microturbulence ($\xi_{\rm micro}$; in the case of 1D stellar atmospheres). With the advent of larger telescopes and major advancement in the instruments that efficiently record spectra in the visual or optical wavelength regime, huge progress has been made in the spectroscopic analysis techniques for estimating

accurate fundamental stellar parameters (see, e.g., Jofré et al. 2019). This has also led to advances in large-scale analyses of optical spectroscopic surveys such as Gaia/GSPspec (Recio-Blanco et al. 2023), Galactic archaeology with HER-MES/GALAH (Buder et al. 2021), the large sky area multiobject fiber spectroscopic telescope/LAMOST (He et al. 2017), Gaia-ESO (Randich et al. 2022), and several others that observe and analyze the stellar spectra of millions of stars of different spectral types and at various evolutionary stages. These surveys provide reliable stellar parameters and abundances mainly for the relatively warmer FGK type stars ($T_{\rm eff} > 4000$ K; Jofré et al. 2019), however, the optical spectra of the ubiquitous cooler M-type stars are riddled by diatomic (e.g., TiO, FeH, OH, and CO) and triatomic (e.g., H2O) molecules in their atmospheres, which makes their optical spectra nearly impossible to analyze.

Department of Astronomy and McDonald Observatory, The University of Texas, 2515 Speedway, Austin, TX 78712, USA

^{*} Data table is only available at the CDS via anonymous ftp to cdsarc.cds.unistra.fr (130.79.128.5) or via https://cdsarc.cds.unistra.fr/viz-bin/cat/J/A+A/675/A23

The spectra of M-type stars in the near-infrared (NIR) wavelength regime $(0.75-2.4\,\mu\text{m})$ can be analyzed, however. This opens up the possibility to use these stars in spectroscopic analyses and to use them as probes for the study of stellar populations. In addition, stars in the direction of high extinction are preferably analyzed in the infrared. For instance, spectroscopic investigations of stars in the highly dust enshrouded Galactic center region demand observations at NIR wavelengths and also limit the observable stellar populations to the relatively brighter M-giant stars. This calls for the development of spectroscopic techniques for determining reliable stellar parameters from spectra recorded at NIR wavelengths as well. With the immense possibility of observing more distant M giants with upcoming large telescopes such as the Extremely Large Telescope/ELT (de Zeeuw et al. 2014) and Thirty Meter Telescope/TMT (Skidmore 2022) and the high-resolution NIR spectroscopic instruments projected for them (Maiolino et al. 2013; Genoni et al. 2016; Mawet et al. 2019), there is an urgent need to develop methods for deriving reliable stellar parameters from NIR spectra of M giants.

Existing methods for determining the effective temperatures, $T_{\rm eff}$, of M giants such as those based on interferometry (Mozurkewich et al. 2003), the infrared flux method (IRFM; Casagrande 2008), and the color- $T_{\rm eff}$ relation (Bessell et al. 1998) are limited to nearby stars and are also subjected to uncertainties arising from interstellar reddening. Thus, the determination of $T_{\rm eff}$ using these methods is less useful for the distant and highly extinct stars in the inner Milky Way regions, and methods are required that can directly extract stellar parameters from NIR spectra. Methods like this for GK stars $(T_{\text{eff}} > 4000 \text{ K})$ that use the ratios of the depths between low- and high-excitation lines (i.e., line depth ratios; Gray 2008) have been attempted in recent studies (Fukue et al. 2015; Taniguchi et al. 2018, 2021; Matsunaga et al. 2021; Afşar et al. 2023), but were found to be affected by metallicity and abundance ratios (Jian et al. 2019). Ryde & Schultheis (2015) and Schultheis et al. (2016) determined T_{eff} for M giant stars in the solar neighborhood and the Galactic center by using the spectral indices of the CO band heads in low-resolution K-band spectra, and Thorsbro et al. (2018, 2020) used the spectral indices of K-band scandium lines. Similarly, Ghosh et al. (2019, 2021, 2022) determined the metallicity-dependent $T_{\rm eff}$ -equivalent width relations using lowresolution H- and K- band spectra of cool stars. These methods need further refinement and tests using reliable benchmark stars, however.

Similarly, asteroseismology, which is considered to be a reliable method for determining the surface gravities, $\log g$, of giants, is currently only tested for warmer giants (Pinsonneault et al. 2018) and also needs repeated high-quality observations. Another way is to use the fundamental relation of $\log g$ (Nissen et al. 1997), which demands reliable values of the mass, luminosity, stellar radius, and distance measurements,

$$\log \frac{g}{g_{\odot}} = \log \frac{M}{M_{\odot}} - 4 \log \frac{T_{\text{eff}}}{T_{\text{eff}_{\odot}}} + 0.4(M_{\text{bol}} - M_{\text{bol}_{\odot}}), \tag{1}$$

where M is the stellar mass, $T_{\rm eff}$ is the effective temperature, and $M_{\rm bol}$ is the absolute bolometric magnitude estimated from the distance modulus relation. This is again only possible for bright nearby stars with reliable parallax measurements from astrometry missions such as the *Gaia* mission (Gaia Collaboration 2021). This necessitates the development of other methods for determining the surface gravity from the NIR spectra of distant M giants.

In this paper, we present an iterative method using the tool called spectroscopy made easy (SME; Valenti & Piskunov 1996, 2012) to determine reliable stellar parameters of cool M giants $(3400 \lesssim T_{\rm eff} \lesssim 4000 \, {\rm K})$ in the solar neighborhood from NIR H-band spectra. We demonstrate the method by using IGRINS spectra at a spectral resolving power of $R \sim 45\,000$ and make use of $T_{\rm eff}$ sensitive molecular OH lines in combination with CO molecular bands and Fe lines. The details of the observations and data reduction procedure are described in Sect. 2. In Sect. 3 we briefly describe the line list we used, and in Sect. 4 we describe the iterative method we used to determine stellar parameters for six nearby well-studied M giants based on spectra from the IGRINS spectral library (Park et al. 2018; Sawczynec et al. 2022) in Sect. 5. We show the quality of our parameter estimates by comparing the determined $T_{\rm eff}$ with reliable values in the literature (from interferometry and photometric and spectroscopic methods) and if available, $\log g$ and [Fe/H]. With this method, we then determine the stellar parameters and α -element abundances of 44 solar neighborhood M giants that are also observed by the NIR spectroscopic survey Apache Point Observatory Galactic Evolution Experiment (APOGEE; Holtzman et al. 2018; Jönsson et al. 2018). In Sect. 5 we also compare the stellar parameters and the α -element abundance trends with respect to APOGEE and other literature sources. The final conclusions are given in Sect. 7.

2. Observations and data reduction

We analyzed NIR spectra of 50 M giants observed with the Immersion GRating INfrared Spectrograph (IGRINS; Yuk et al. 2010; Wang et al. 2010; Gully-Santiago et al. 2012; Moon et al. 2012; Park et al. 2014; Jeong et al. 2014). IGRINS provides spectra spanning the full H and K bands (1.45–2.5 µm) with a spectral resolving power of $R \sim 45\,000$. We carried out new observations of 44 M giant stars with IGRINS mounted on the Gemini South telescope (Mace et al. 2018) within the programs GS-2020B-Q-305 and GS-2021A-Q302. The observations were performed in service mode in January to April 2021. Details of the observations are listed in the Table 1. We also analyzed the IGRINS spectra of 6 nearby M giants available in the IGRINS spectral library (Park et al. 2018; Sawczynec et al. 2022), which we present in Table 2.

The IGRINS observations were carried out in one or more ABBA nod sequences along the slit, permitting sky background subtraction. The exposure times were set to aim at an average signal-to-noise ratio (S/N) of at least 100, leading to observing times ranging from 5 to 25 min. The S/N provided by the Raw & Reduced IGRINS Spectral Archive (RRISA; Sawczynec et al. 2022) is the average S/N for the *H* or *K* band, and is given per resolution element. It varies over the orders and is lowest at the end of the orders. In all cases except for a few, an S/N above 100 was achieved (see the last column in Table 1). For one-third of the observations, the S/N is two to three times higher because the weather was better than expected.

We used the IGRINS pipeline package (IGRINS PLP; Lee et al. 2017) to optimally extract the wavelength-calibrated spetra that are corrected for telluric lines after flat-field correction and A-B frame subtraction. The spectral orders of the science targets and the telluric standards were subsequently stitched together after normalizing every order and then combining them in iraf (Tody 1993), excluding the low S/N edges of every order. This resulted in one normalized stitched spectrum for the entire *H* and *K* bands. However, to take any modulations in the continuum levels of the spectra into account, we defined

Table 1. Observational details of K giant stars.

Index	2MASS ID	H _{2MASS} (mag)	K _{2MASS} (mag)	Date UT	Exposure time mm:ss	SNR _H (per reso	SNR _K lution element)
1	2M05484106-0602007	7.0	6.7	2021-01-02	06:32	110	130
2	2M05594446-7212111	7.0	6.8	2021-01-02	10:35	100	120
3	2M06035110-7456029	7.0	6.7	2021-01-01	13:25	90	110
4	2M06035214-7255079	7.1	6.8	2021-01-01	06:04	100	110
5	2M06052796-0553384	7.0	6.6	2021-01-02	07:08	100	120
6	2M06074096-0530332	7.3	6.5	2021-01-02	08:22	90	130
7	2M06124201-0025095	7.0	6.7	2021-01-01	07:34	90	100
8	2M06140107-0641072	7.2	6.8	2021-01-02	06:02	50	65
9	2M06143705-0551064	7.2	6.9	2021-01-02	07:13	70	90
10	2M06171159-7259319	7.2	6.9	2021-01-02	06:21	120	130
11	2M06223443-0443153	7.1	6.8	2021-01-02	08:35	90	110
12	2M06231693-0530385	7.1	6.7	2021-01-02	08:05	80	100
13	2M06520463-0047080	7.1	6.7	2021-01-02	06:41	80	100
14	2M06551808-0148080	7.1	6.8	2021-01-02	04:10	90	100
15	2M06574070-1231239	7.3	6.9	2021-01-02	09:31	90	110
16	2M10430394-4605354	7.2	6.9	2021-02-11	06:22	120	120
17	2M11042542-7318068	7.2	6.9	2021-02-11	05:50	120	130
18	2M12101600-4936072	7.2	6.9	2021-02-19	06:28	70	90
19	2M13403516-5040261	7.1	6.8	2021-03-17	11:27	170	170
20	2M14131192-4849280	7.2	6.9	2021-03-17	09:02	150	150
21	2M14240039-6252516	6.6	6.2	2021-03-18	12:36	240	250
22	2M14241044-6218367	7.3	6.8	2021-04-17	09:38	230	260
23	2M14260433-6219024	7.2	6.8	2021-02-18	05:01	50	70
24	2M14261117-6240220	7.0	6.5	2021-02-14	08:09	80	100
25	2M14275833-6147534	7.0	6.5	2021-02-18	05:19	80	100
26	2M14283733-6257279	6.5	6.1	2021-02-18	06:59	70	90
27	2M14291063-6317181	7.4	6.9	2021-02-18	05:16	80	110
28	2M14311520-6145468	7.3	6.7	2021-04-20	06:32	150	170
29	2M14322072-6215506	6.7	6.4	2021-04-13	11:40	270	290
30	2M14332169-6302108	6.9	6.5	2021-04-13	05:45	120	130
31	2M14332169-6302166 2M14332869-6211255	6.5	6.1	2021-04-20	06:20	120	140
32	2M14333081-6221450	7.2	6.7	2021-02-20	10:10	210	240
33	2M14333688-6232028	7.2	6.8	2021-03-18	14:24	210	250
34	2M14345114-6225509	7.2	6.6	2021-04-24	13:55	270	300
35	2M14360142-6228561	6.4	6.0	2021-04-20	10:23	80	90
36	2M14360935-6309399	6.9	6.5	2021-04-20	06:40	90	100
37	2M14371958-6251344	6.7	6.3	2021-04-20	09:18	240	240
38	2M14371938-6231344 2M14375085-6237526	7.3	7.0	2021-04-24	07:49	100	120
39	2M15161949+0244516	7.3	7.0	2021-04-20	14:01	190	190
40		7.2	6.5	2021-04-24	08:21	200	290
	2M17584888-2351011				08:21 08:47		
41	2M18103303-1626220	7.3	6.5	2021-04-28		230	310
42	2M18142346-2136410	7.1	6.6	2021-04-28	12:19	240	280
43	2M18191551-1726223	7.2	6.6	2021-04-28	14:16	320	380
44	2M18522108-3022143	7.3	6.9	2021-04-28	24:03	320	320

specific local continua around the spectral line that was studied. This was an important measure for accurate determinations of the α element abundances (see, e.g., Santos-Peral et al. 2020). In the subsequent abundance analysis, we also allowed for wavelength shifts in order to fit the lines in the line masks we used. This takes any errors or trends in the wavelength solution into account.

The standard procedure for eliminating the contaminating telluric lines is to divide by a telluric standard-star spectrum that only shows telluric lines and mostly no stellar features. In the IGRINS observing strategy, telluric stars were chosen to be fast-rotating late-B to early-A dwarfs that were observed close in time and at an air mass similar to that of the science targets.

This procedure worked very well for most wavelength regions. Except for some broad Brackett lines of hydrogen¹, some spurious broadband spectral features might be in the telluric standard-star spectrum, however special attention was given to the lines in these regions.

Broad absorption features caused by diffuse interstellar bands (DIBs; see, e.g., Geballe 2016) might also appear in high-resolution spectra. These are probably due to large molecules in the interstellar medium (ISM) in the line of sight of the star. The DIBs are often weak and normally correlate with the reddening, $E_{(B-V)}$. They are therefore mainly found in

Brackett (n = 7) line at 2166 nm.

Table 2. Fundamental stellar parameters estimated from the IGRINS spectra of six benchmark stars using our method and the literature compilation of stellar parameters (indicated by the *lit* subscript).

Star	V	$K_{2\text{MASS}}$	E(B-V)	$T_{\rm eff}$ (K)	$T_{\mathrm{eff}\ lit}\left(\mathrm{K}\right)$	$\log g (\mathrm{dex})$	$\log g_{lit}$ (dex)	[Fe/H] (dex)	[Fe/H] lit (dex)
HD 132813	4.54	-0.96	0.02	3457	$3410 \pm 37^{(1)}$ $3406^{(2)}$	0.43	- 0.53 ⁽²⁾	-0.27	-
					$3387 \pm 39^{(3)}$ $3458^{(4)}$		0.46 ± 0.25 ⁽³⁾		-0.09 ± 0.18 ⁽³⁾
HD 89758	3.05	-1.01	0.01	3807	3868 ± 37 ⁽¹⁾	1.15		-0.09	
					$3793 \pm 50^{(5)}$		$1.07 \pm 0.10^{(5)}$		$-0.34 \pm 0.10^{(5)}$
					$3822 \pm 43^{(3)}$		$1.39 \pm 0.17^{(3)}$		-0.20 ± 0.06 ⁽³⁾
					3777 ⁽⁴⁾		_		_
HD 175588	4.3	-1.25	0.11	3484	3394 ± 32 ⁽¹⁾	0.49	_	-0.04	_
					3408 (2)		_		_
					$3484 \pm 16^{(3)}$		$0.47 \pm 0.17^{(3)}$		$-0.14 \pm 0.16^{(3)}$
					3487 ⁽⁴⁾		_		_
HD 224935	4.41	-0.40	0.04	3529	$3490 \pm 35^{(1)}$	0.64	_	-0.10	_
					3504 ⁽²⁾		_		_
					3592 ⁽⁴⁾		-		-
HD 101153	5.36	-0.21	0.04	3438	$3421 \pm 35^{(3)}$	0.51	0.48 ± 0.25 (3)	-0.07	$-0.09 \pm 0.12^{(3)}$
					$3418 \pm 100^{(6)}$		0.49 ± 0.25 ⁽⁶⁾		$0.00 \pm 0.10^{(6)}$
					3455 ⁽⁴⁾		_		_
HD 96360	8.09	2.77	0.02	3459	3432 (2)	0.5	_	-0.15	_
					$3471 \pm 22^{(3)}$		$0.8 \pm 0.23^{(3)}$		$0.0 \pm 0.17^{(3)}$
					$3550 \pm 100^{(6,7)}$		0.72 ± 0.25 ^(6,7)		$-0.37 \pm 0.10^{(6,7)}$
					3484 (4)		_		_

Notes. We list $\log g$ and [Fe/H] values as '–' if there are no $\log g$, [Fe/H] measurements in the literature (e.g., in the case of optical interferometric measurements as in Baines et al. 2021 or $T_{\rm eff}$ versus (V-K)₀ relation in Bessell & Brett 1988). **References.** ⁽¹⁾Baines et al. (2021), ⁽²⁾Lebzelter et al. (2019), ⁽³⁾Sharma et al. (2016), ⁽⁴⁾ $T_{\rm eff}$ from Bessell et al. (1998) V-K relation, ⁽⁵⁾Jönsson et al. (2014), ⁽⁶⁾Guerço et al. (2019), ⁽⁷⁾Smith & Lambert (1990).

spectra of reddened stars. Most DIBs have been identified in optical spectra, but some are found in the NIR (Geballe et al. 2011), and more are being identified with new instruments (e.g., with X-shooter, APOGEE, IGRINS, WINERED, and CRIRES in Cox et al. 2014; Elyajouri et al. 2017; Galazutdinov et al. 2017; Hamano et al. 2022; Ebenbichler et al. 2022, respectively). None of these known DIBs are close to the spectral lines that we use in the following discussion.

Finally, for the wavelength solutions, sky OH emission lines were used (Han et al. 2012; Oh et al. 2014), and the spectra were subsequently shifted to laboratory wavelengths in air after a correction for the stellar radial velocity. In addition, we removed obvious cosmic-ray signatures from the spectra.

3. Analysis

We carried out the spectral synthesis using the code called spectroscopy made easy (SME; Valenti & Piskunov 1996, 2012). SME generates synthetic spectra by calculating the spherical radiative transfer through a relevant stellar atmosphere model defined by its fundamental stellar parameters. SME finds this model by interpolating in a grid of one-dimensional (1D) model atmospheres in a radiative and convective scheme (MARCS) stellar atmosphere models (Gustafsson et al. 2008). These are hydrostatic model atmospheres in spherical geometry, computed assuming LTE, chemical equilibrium, homogeneity, and conservation of the total flux. In order to account for the non-LTE (NLTE) effects, we used an NLTE grid for which the departure coefficients were computed using the MPI-parallelized NLTE radiative transfer code Balder (Amarsi et al. 2018). The NLTE grids for Si, Mg, and Ca were taken from Amarsi et al. (2020) and those for Fe from Amarsi et al. (2016) and Lind et al. (2017) (with subsequent updates; Amarsi priv. comm.). SME applies departure coefficients by interpolating in these grids.

As a line list, we used an updated version of the VALD line list (Piskunov et al. 1995; Kupka et al. 2000; Ryabchikova et al. 2015). The transition probability (gf-values, i.e., the product of the statistical weight and the oscillator strength) of the lines lacking reliable experimental gf-values was determined astrophysically using the high-resolution infrared solar flux spectrum of Wallace & Livingston (2003) that was tested for Arcturus (α boo) using the high-resolution ($R \sim 100\,000$) infrared spectrum from the Arcturus atlas (Hinkle et al. 1995), and adopting the stellar parameters from Ramírez & Allende Prieto (2011). In the astrophysical determination of the gf-values, we set the abundance of an element to a reference value (0.0 in the case of the Sun, and 0.37 from Ramírez & Allende Prieto 2011 for Arcturus) and fit a synthetic spectrum to the absorption line in the observed spectrum of the Sun or Arcturus by varying the gf-value.

For many lines, we adopted the broadening parameters (corresponding to the collisional broadening due to neutral hydrogen, and in some cases, charged particles) from the ABO theory (Anstee & O'Mara 1991, 1995; Barklem & O'Mara 1997; Barklem et al. 1998) or from the spectral synthesis code BSYN based on routines from MARCS (Gustafsson et al. 2008). Details of the calculation of the broadening parameters for the magnesium multiplet lines in the *K* band can be found in Nieuwmunster et al. (2023).

A detailed validation of the line list was carried out using the IGRINS H- and K-band spectra of \sim 40 solar neighborhood K giants in the sample called giants in the local disk (GILD; Jönsson et al., in prep., which builds upon and improves the analysis described in Jönsson et al. 2017). The stellar parameters and abundances for stars in the GILD sample were determined from optical FIES spectra. The line list we used was validated by comparing the elemental abundance trends determined from

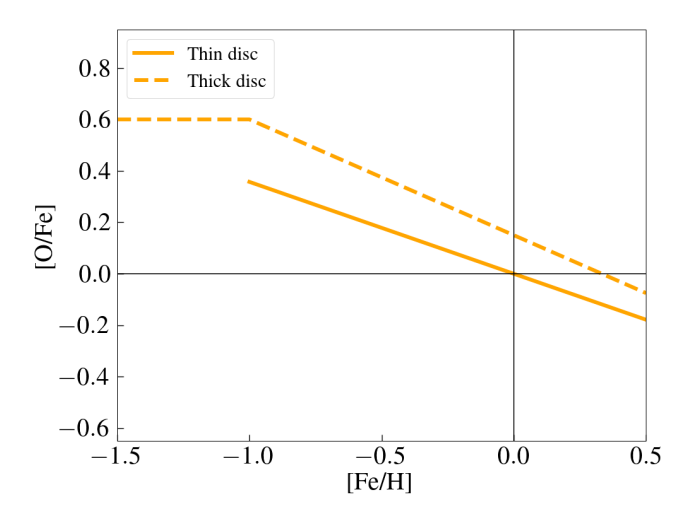


Fig. 1. Simple functional form of the [O/Fe] vs. [Fe/H] trend for thinand thick-disk stellar populations (or low- α and high- α populations; see Minchev et al. 2017) adopted from Amarsi et al. (2019).

IGRINS NIR absorption lines for the above-mentioned K giants with the trends for the same stars determined in GILD with a reliable optical line list (Nandakumar et al., in prep.). The line list we used was used in Montelius et al. (2022), Nandakumar et al. (2022); and Nieuwmunster et al. (2023). Thus we used a line list with selected and reliable lines that were tested not only on the Sun and the Arcturus, but also on \sim 40 solar neighborhood K giants.

The line data for the CO, CN, and OH molecular lines were adopted from the line lists of Li et al. (2015), Brooke et al. (2016), and Sneden et al. (2014), respectively. The central wavelengths and gf values of the selected OH, CN, and CO molecular lines we used in the stellar parameter estimation method (see Sect. 4) are listed in the Tables A.3–A.5, respectively. The central wavelengths, VALD, or astrophysically calibrated gf values and broadening parameters of Mg, Si, Ca, Ti, and Fe are listed in Table A.2.

4. Method

An accurate determination of the effective temperature, T_{eff} , is crucial in spectroscopic analyses becaus $T_{
m eff}$ defines the energy that is transported through a star. It therefore shapes the continuum of the stellar spectrum, the excitation balance of lines, and the ionization stages of elements. Hence, we started by identifying T_{eff} -sensitive absorption lines in the H-band regime that can be used to constrain $T_{\rm eff}$. We chose a random set of 236 stars from the APOGEE DR17 catalog within 100 K bins between $3000 \text{ K} < T_{\text{eff}} < 4500 \text{ K}$, and 0.5 dex bins between-1.5 < [Fe/H] < 0.5 dex. Based on visual inspection of APOGEE spectra of stars with different T_{eff} but similar set of $\log g$, [Fe/H], ξ_{micro} , and so on, we identified a set of ~50 molecular OH lines that are sensitive to $T_{\rm eff}$. We further selected a subset of 15–20 OH lines from which we were able to recover the APOGEE $T_{\rm eff}$ within ± 100 K when we ran SME with $T_{\rm eff}$ set as a free parameter for the 236 stars. In addition to $T_{\rm eff}$, the strength of these lines also depends on the oxygen (O) abundance. Thus, it is necessary for this method that the O abundance is known or fixed in order to constrain the $T_{\rm eff}$ from the OH lines.

Amarsi et al. (2019) derived 3D NLTE O abundances for 187 F and G dwarfs belonging to thin-disk, thick-disk and halo stars of the Milky Way. Based on their Fig. 12 (left panel), we made functional forms of the [O/Fe] versus [Fe/H] trend for thin

and thick disc stars, as shown in Fig. 1. We used these functional forms of the trends to fix [O/Fe] for stars with any metallicity belonging to the thin or thick-disk (It would be more correct to call these populations low- α population instead of thin-disk population and high- α population instead of thick-disk population; see, e.g., Minchey et al. 2017).

In addition to the OH lines, we chose a set of CN and CO lines (including molecular band heads) and Fe lines as listed in Tables A.4, A.5, and A.2, respectively. This constrained the molecular equilibrium of C-, N-, and O-bearing molecules, and the metallicity.

As the first assumption, we categorized the stars into thin- or thick-disk stars. We then assumed a starting T_{eff} and [Fe/H] of 3500 K and 0.00 dex. For this $T_{\rm eff}$ and [Fe/H], we obtained a log gof 0.65 for a 10 Gyr old star from the Yonsei-Yale isochrones by means of simple linear interpolation (see also Rich et al. 2017). At this metallicity, [O/Fe] is 0.0 for a thin-disk star and 0.15 for a thick-disk star. In the initial step, we ran SME by setting $T_{\rm eff}$, [Fe/H], ξ_{micro} , and the C and N abundances as free parameters for the selected set of lines. SME generated and fits multiple synthetic spectra for all the chosen lines of interest for different combinations of the free parameters. The final values of the parameters were determined from the model with the best fits of the chosen lines by means of a χ^2 minimization between the synthesized and the observed spectrum in the marked regions of the chosen spectral lines. This initial step resulted in a new set of $T_{\rm eff}$ and [Fe/H] that were used to constrain $\log g$ from the Yonsei-Yale (YY) isochrones assuming old ages of 3–10 Gyr (Demarque et al. 2004). In the next SME run, we used the $T_{\rm eff}$, [Fe/H], ξ_{micro} , and the C and N abundances from the previous run, $\log g$ from the YY isochrone tracks, and [O/Fe] at the new [Fe/H] based on the trend in Fig. 1. This cycle was repeated until the difference between values of all free parameters from the current SME run and the previous SME run was negligible. In Fig. 2 we show the flow diagram indicating the sequence of steps followed in the method.

While $T_{\rm eff}$ and [Fe/H] are mainly constrained by the OH lines and Fe lines, respectively, different sets of weak and strong lines help us to constrain the $\xi_{\rm micro}$. Inclusion of CO and CN lines not only constrains the C and N abundances, but also results in an excellent synthetic spectra fit to the observed CN and CO lines and thus takes the CN and CO blends into account as well. At the same time, when we carried out the entire exercise excluding the CN, CO lines and thus removed C and N from the set of free parameters, the difference in all stellar parameter values was negligible except for [Fe/H] which was found to vary within 0.1 dex. This might be an indication of possible CN and/or CO blends in the Fe lines we selected.

5. Validation of the method

In this section, we validate the method we described in the previous section by determining stellar parameters for 6 nearby M giants (see Sect. 5.1.1), some of which have reliable parameters in the literature. We then use the method to determine stellar parameters for 44 solar neighborhood M giants (see Sect. 5.1.2) followed by a discussion of the uncertainties (see Sect. 5.2). We later determine the α abundance trends from selected Mg, Si, Ca, and Ti lines (Sect. 6), which further proves the usefulness of the method by showing the precision and accuracy of the abundance trends compared to those determined based on other methods.

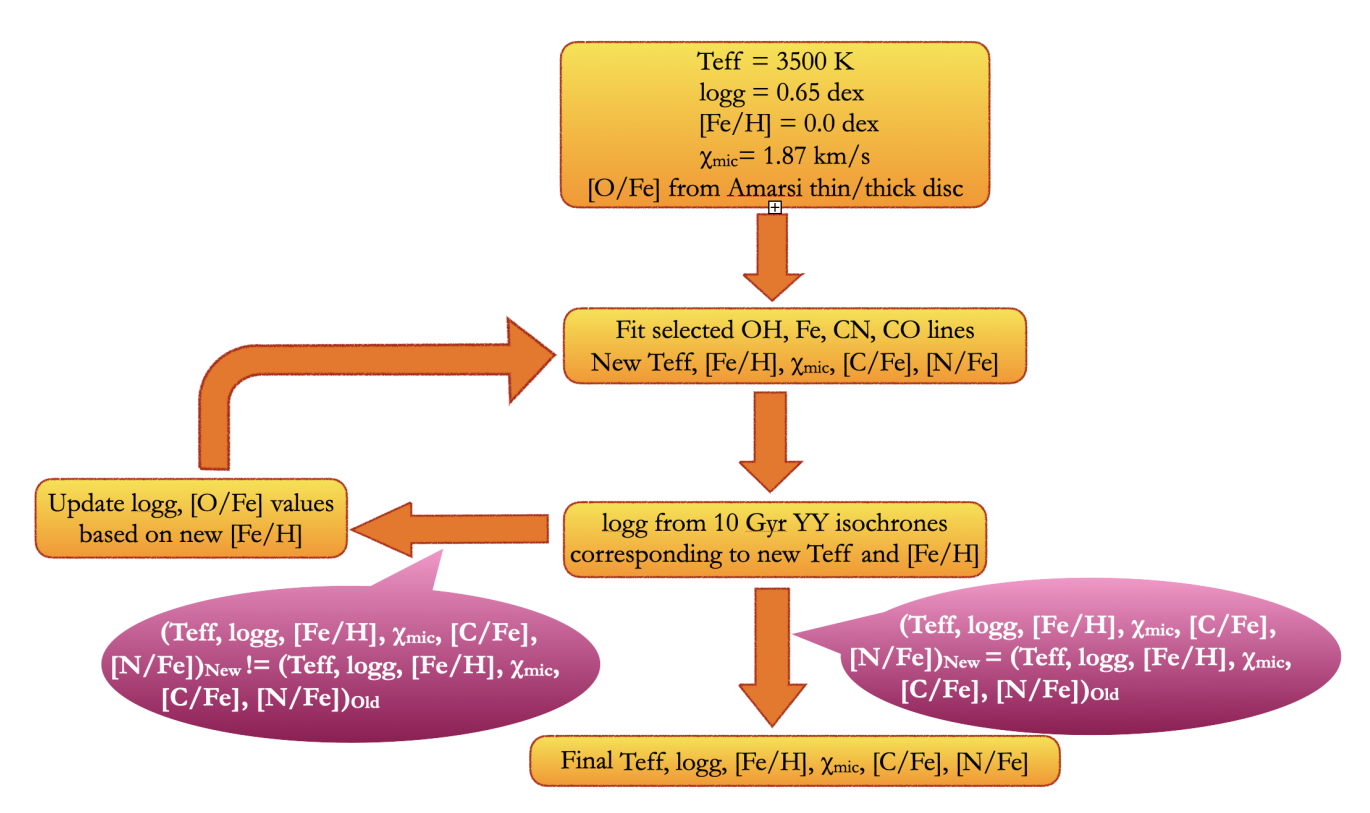


Fig. 2. Flow diagram of the method with which we determined reliable stellar parameters of the cool M giants ($3400 \lesssim T_{\rm eff} \lesssim 4000 \, {\rm K}$) from NIR H-band spectra.

5.1. Stellar parameters

5.1.1. Nearby M giants

As a test case of our method, we selected six nearby M giants, the H- and K-band spectra of which are available in the IGRINS spectral library (Park et al. 2018; Sawczynec et al. 2022). We compiled their T_{eff} , $\log g$, and [Fe/H], derived using different methods from various literature sources. The $T_{\rm eff}$ for four of these stars (HD 132813, HD 89758, HD 175588, and HD 224935) was estimated based on the very precise angular diameter measurements using the Navy Precision Optical Interferometer (NPOI) in combination with distances from Gaia parallaxes (Baines et al. 2021). These values of $T_{\rm eff}$ are therefore very accurate and reliable. Furthermore, we also used the $T_{\rm eff}$ for the four stars (HD 132813, HD 175588, HD 224935, and HD 96360) from Lebzelter et al. (2019), estimated using the $T_{\rm eff}$ – (V – K) relation derived from a homogeneous set of angular diameters by Richichi et al. (1999). They also estimated $\log g$ for one star (HD 132813) using the fundamental relation of $\log g$ assuming a mass of $1.2 M_{\odot}$ and the luminosity and distances from *Gaia*. Unlike the above-mentioned studies, Sharma et al. (2016) provided all three stellar parameters for five stars (HD 132813, HD 89758, HD 175588, HD 101153, and HD 96360) based on a full spectrum fitting of 331 stars in the MILES and ELODIE spectral libraries, making use of the newer version, V2, of the MILES interpolator and the spectrum fitting tool, ULySS. For one star (HD 89758), we found all three stellar parameters in Jönsson et al. (2014) with the $T_{\rm eff}$ provided from angular diameter measurement by Mozurkewich et al. (2003), log g estimated using the fundamental relation, and [Fe/H] determined from Fe I lines in a visual spectrum from the ELODIE spectral archive. For HD96360, Smith & Lambert (1990) estimated T_{eff} based on the T_{eff} -spectral-type relation from Tsuji (1981), $\log g$ using the fundamental relation assuming a mass of $1.5\,M_\odot$, and [Fe/H] as the mean of the Ti, Fe, and Ni abundances. These parameters were adopted by Guerço et al. (2019), who also provided all three stellar parameters for HD 101153 with, in this case, the $T_{\rm eff}$ estimated using the $T_{\rm eff}$ – (V – K) $_0$ relation from Bessell et al. (1998), log g using the PARAM 1.3 code, and [Fe/H] determined using a sample of 19 Fe I lines in the K-band wavelength regime. Finally, for all six stars, we determined $T_{\rm eff}$ using the following $T_{\rm eff}$ – (V – K) $_0$ relation from Bessell et al. (1998):

$$T_{\text{eff}} = 9102.523 - 3030.654(V - K)_0 + 633.3732(V - K)_0^2 - 60.73879(V - K)_0^3 + 2.135847(V - K)_0^4.$$
 (2)

By using the Python package dustmaps², we estimated the dereddened values of V and K for this equation, with the reddening values ($E_{(B-V)}$) from the two-dimensional map of dust, constructed by Schlegel et al. (1998) based on far-infrared emission of dust. We used conversion factors of 3.07 and 0.366 to determine the extinctions $A_{\rm V}$ and $A_{\rm K}$, respectively (see Table A1 in Casagrande & VandenBerg 2014).

We also determined the stellar parameters for these stars with our method using IGRINS H-band spectra and assuming that the stars belong to the thin-disk stellar population. Table 2 lists the stellar parameters for all six stars determined with our method, along with the V, $K_{2\text{MASS}}$ and $E_{(B-V)}$ values, as well as the stellar parameters from the literature. In Fig. 3 we plot the difference in stellar parameters (literature – IGRINS) as a function of our IGRINS parameters. The differences in T_{eff} for comparisons with multiple literature sources lie well within $\pm 100\,\text{K}$, with a minimum difference seen when compared to T_{eff} derived using the Bessell et al. (1998) relation for all six stars. The differences in $\log g$ are largest for HD96360 and HD89758 when

https://dustmaps.readthedocs.io/en/latest/

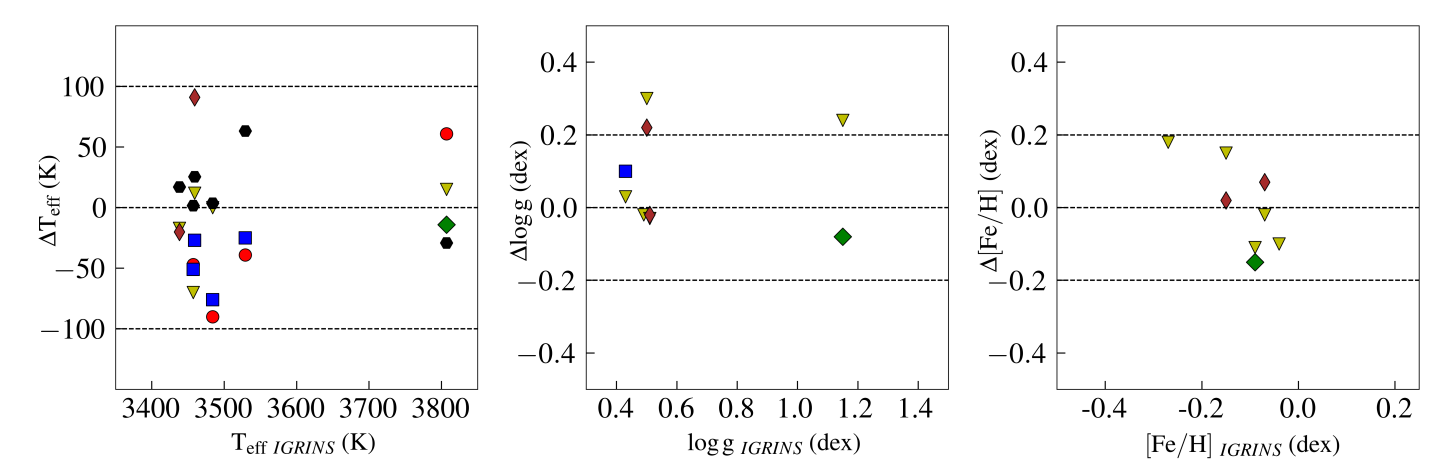


Fig. 3. Difference (literature – this work) in $T_{\rm eff}$ (left panel), log g (middle panel), and [Fe/H] (right panel) on the y-axis vs. the respective parameter estimates using our method (x-axis) for the six nearby M giant stars in the IGRINS spectral library. Differently colored symbols represent the compiled literature estimates: red circles show Baines et al. (2021), blue squares show Lebzelter et al. (2019), green diamonds show Jönsson et al. (2014), inverted yellow triangles show Sharma et al. (2016), and brown diamonds show Guerço et al. (2019). The black circles denote the $T_{\rm eff}$ estimated using the $T_{\rm eff}$ vs. (V-K) $_0$ relation in Eq. (2) (from Bessell et al. 1998). $K_{\rm 2MASS}$ has been corrected to the photometric system in Bessell & Brett (1988; https://irsa.ipac.caltech.edu/data/2MASS/docs/releases/allsky/doc/sec6_4b.html)

compared to the values from Sharma et al. (2016) with uncertainties of \sim 0.2 dex. We would like to point out that the remaining stars with available $\log g$ have small differences that lie within 0.1 dex. The differences in [Fe/H] also lie within levels of \pm 0.2 dex, which is also comparable to the uncertainties in the measurements in the literature. Overall, the agreement for all three stellar parameters we determined using our method for the six well-studied nearby M giants is therefore good. This is a clear indication of the efficiency of our method for determining accurate stellar parameters for M giants.

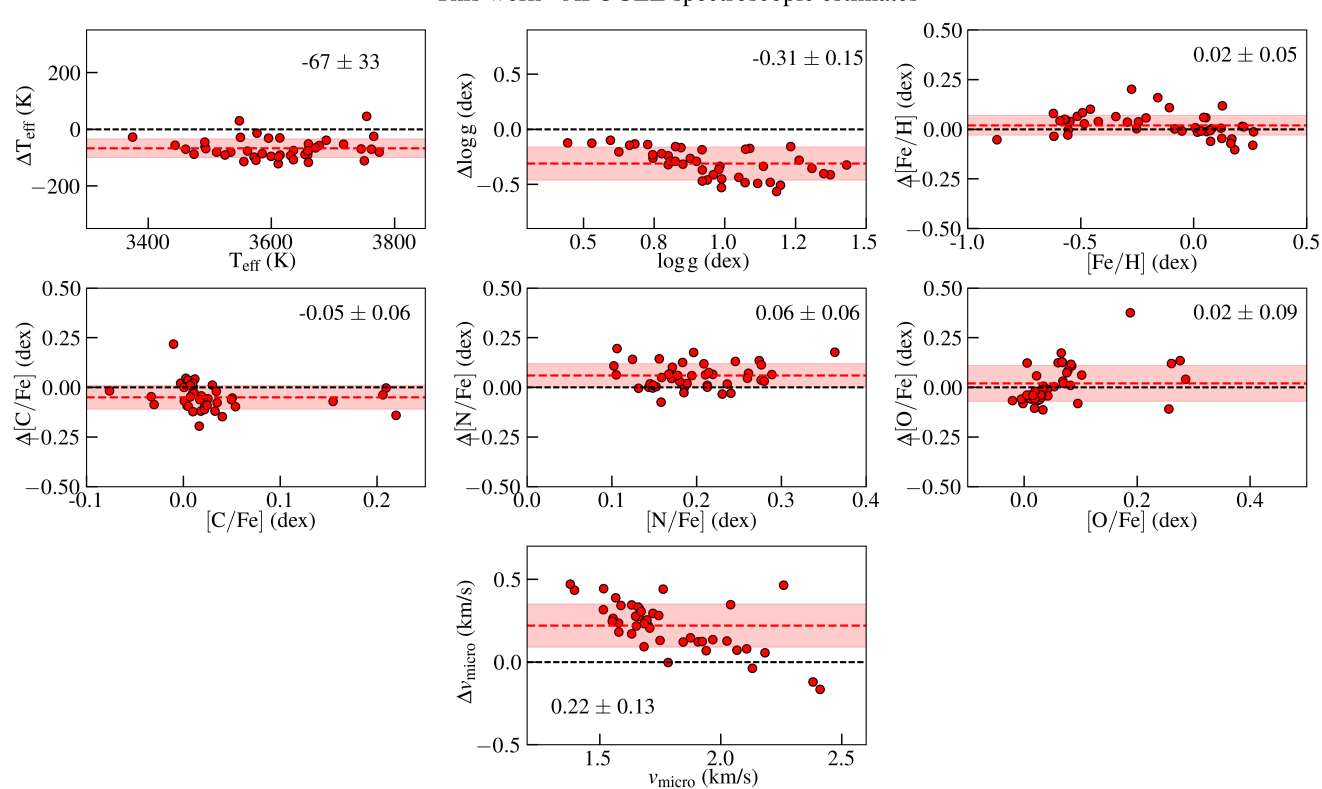
5.1.2. Solar neighborhood M giants

Next, we applied our method to our new IGRINS spectra of the 44 solar neighborhood M giants. All 44 stars were also observed by the APOGEE survey. Their stellar parameters and individual elemental abundances are available in the latest data release, DR17, for all stars except one (39). We identified 5 stars that belong to the thick-disk population based on their enhanced APOGEE magnesium abundance from the [Mg/Fe] versus [Fe/H] plot. Thus, we fixed the oxygen abundance for these 5 stars according to the thick-disk trend and for the remaining 40 stars according to the thin-disk trend in Fig. 1. Later, based on our abundance analysis (alpha abundances), star 39 was identified to be a thick-disk star. When we re-estimated the parameters assuming the thick-disk oxygen trend (an increase of 0.17 dex in [O/Fe]), we found a 110 K increase in $T_{\rm eff}$, a 0.23 dex increase in $\log g$, a 0.07 dex decrease in [Fe/H], a $0.2 \,\mathrm{km} \,\mathrm{s}^{-1}$ increase in ξ_{micro} , a 0.14 dex increase in [C/Fe], and a 0.07 dex increase in [N/Fe]. It is surprising and reassuring that even after the initial misidentification, we were able to correctly deduce the correct population based on the abundances we derived using the incorrect stellar parameters. Nevertheless, it is an encouraging sign that there are ways to identify and correct these incorrect initial assumptions (see the further discussion in the section on uncertainties, Sect. 5.2). Stellar parameters, [C/Fe], [N/Fe], assumed [O/Fe] and stellar populations for each star are listed in the Table 3.

APOGEE derived $T_{\rm eff}$, $\log g$, [Fe/H], $\xi_{\rm micro}$, $\xi_{\rm macro}$, [C/M], [N/M], [O/M], and the general alpha abundance, [α /M], simultaneously using the APOGEE stellar parameter and chemi-

cal abundance pipeline (ASPCAP; García Pérez et al. 2016) by interpolating in a precomputed grid of synthetic spectra and finding the best-fitting stellar parameters that describe an observed spectrum. In addition to the raw spectroscopic parameters and abundances, APOGEE also provides calibrated values. Because the uncalibrated spectroscopic parameters and abundances are directly derived from the APOGEE spectra, we made use of the spectroscopic parameters (reported under the ASPCAP output array FPARAM) to compare them with the values we derived using our method.

In Fig. 4 we plot the difference in the parameters and abundances (our method - APOGEE) as a function of APOGEE uncalibrated values. We estimated the mean value of the differences and scatter (middle value of the 84th and 16th percentiles), which are listed in each panel. The $T_{\rm eff}$, estimated using our method is lower than the APOGEE T_{eff} for all stars except two: stars 10 and 44. In general, the difference in $T_{\rm eff}$ is small, with a mean of -67 K and scatter of 33 K, thus lying within 100 K for the majority of the stars without significant trends. Similar to $T_{\rm eff}$, the surface gravity, $\log g$, from our method is lower than that of APOGEE, with a mean difference of -0.31 dex and scatter of $0.15 \,\mathrm{dex}$. We also see a trend of lower differences ($<-0.1 \,\mathrm{dex}$) at lower values of APOGEE $\log g$ that increases to ~ -0.5 dex with larger scatter at higher values of APOGEE $\log g$. Holtzman et al. (2018) pointed out that the spectroscopic (raw) $\log g$ values for giants determined by APOGEE ASPCAP are systematically higher than those derived from asteroseismology. This might explain the consistently lower difference we find in $\log g$. At the same time, currently available measurements of asteroseismic $\log g$ are limited to stars with $T_{\rm eff} > 3800 \, \rm K$ (Pinsonneault et al. 2018). Our metallicities agree with the APOGEE metallicities, with a mean difference of 0.02 dex and a small scatter of 0.05 dex. There is a hint of change in the trend in the metallicity differences from positive to negative at higher metallicities, but this cannot be confirmed with the current sample. The difference in ξ_{micro} shows a clear trend, with higher values using our method for lower APOGEE ξ_{micro} , but it tends to agree at higher APOGEE ξ_{micro} . Our ξ_{micro} for a majority of the stars lies in a narrow range of 1.8–2.4 km s⁻¹ and a high value of 2.7 km s⁻¹ for the most metal poor star, star 10. It is encouraging that our values of ξ_{micro} lie in a reasonable range of values



This work - APOGEE spectroscopic estimates

Fig. 4. Differences (this work - APOGEE spectroscopic estimates) in $T_{\rm eff}$, $\log g$, [Fe/H], $\xi_{\rm micro}$, [C/Fe], [N/Fe], and [O/Fe] on the y-axis vs. the APOGEE spectroscopic estimates on the x-axis for the 44 stars in the solar neighborhood from our new IGRINS observations. $T_{\rm eff}$, $\log g$, and [Fe/H] are shown in the three panels in the top row, [C/Fe], [N/Fe], and [O/Fe] in the three panels in the middle row, and $\xi_{\rm micro}$ is plotted in the bottom row panel. The dashed black line indicates the difference value of 0.0 between APOGEE and our estimates. The mean difference and standard deviation (calculated as the middle value of the 84th–16th percentile values for each parameter) is indicated by the dashed red line and the red band, respectively, and is also listed in the respective panels.

that are usually accepted for giants (Smith et al. 2013). Finally, we find small differences for [C/Fe], [N/Fe], and [O/Fe] with respect to APOGEE on average. We note that [C/Fe] from our method is higher for the five thick-disk stars, similar to what APOGEE finds.

Through a further cross match carried out with other large spectroscopic surveys, we found seven stars in the RAVE survey catalog (DR6; Steinmetz et al. 2020) and four stars in the GALAH survey catalog (DR3; Buder et al. 2021). Based on the quality flags, algo_conv_madera (set to 3) in RAVE and flag_sp (not set to 0) in GALAH, these stars do not have reliable stellar parameters determined from their spectra in either survey catalog. The photometric $T_{\rm eff}$ was estimated using the IRFM method (Casagrande et al. 2010) for all five stars in RAVE and for one star in GALAH (Casagrande et al. 2021).

In addition to the comparison with the APOGEE values, we estimated photometric effective temperatures using the $T_{\rm eff}$ -(V-K) relation (Eq. (2)). To do this, we explored the effect of different reddening values. For 11 stars we had $E_{(B-V)}$ from APOGEE directly (set 1, hexagons in Fig. 5), whereas for 21 stars (set 2, crosses in Fig. 5), we adopted the reddening values from Schlegel et al. (1998) renormalized as described in Casagrande et al. (2019). The input photometry being the same, this comparison is a sobering example of how reddening alone can easily introduce a scatter of about ± 50 K for our sample.

In addition to using the above color relation, we also implemented *Gaia* DR3 and 2MASS photometry in the IRFM following Casagrande et al. (2021) by adopting our spectroscopic

values of $\log g$ and [Fe/H] and our renormalized reddening values. To better gauge the uncertainties, for each star, we Monte-Carlo the errors into the IRFM, adopting the quoted uncertainties for the input stellar parameters and photometry, and allowing for an uncertainty in reddening of 10%. For stars with $E_{(B-V)} < 0.85$, our Monte Carlo uncertainties are within $100\,\mathrm{K}$, but they linearly increase to several hundred K for higher reddening values. In order to retain stars with reliably determined IRFM temperatures, we therefore restrict ourselves to stars with $E_{(B-V)}$ below the above threshold, which corresponds to T_{eff} uncertainties in the range $30–60\,\mathrm{K}$. Figure 5 clearly shows that the IRFM values (red diamonds) are consistent with our spectroscopic determinations. The mean difference is $42\,\mathrm{K}$, with a standard deviation of $48\,\mathrm{K}$. We were unable to estimate IRFM temperatures for the six nearby M giants owing to their extreme brightness.

Figure 5 also shows the comparison with the IRFM effective temperatures from RAVE DR6 (Steinmetz et al. 2020). In this version of the IRFM, APASS photometry was used instead, along with log *g* and [Fe/H] derived from RAVE. This comparison shows the effect of the adopted stellar parameters and photometry, with the caveat that *Gaia* DR3 is far superior than APASS. Finally, we also show the comparison with one star with IRFM effective temperature from GALAH that was instead based on the *Gaia* DR2 photometry and transmission curves.

From the different values and methods compared in Fig. 5, we can thus conclude that our effective temperature determinations are reliable, especially in comparison with several others that are

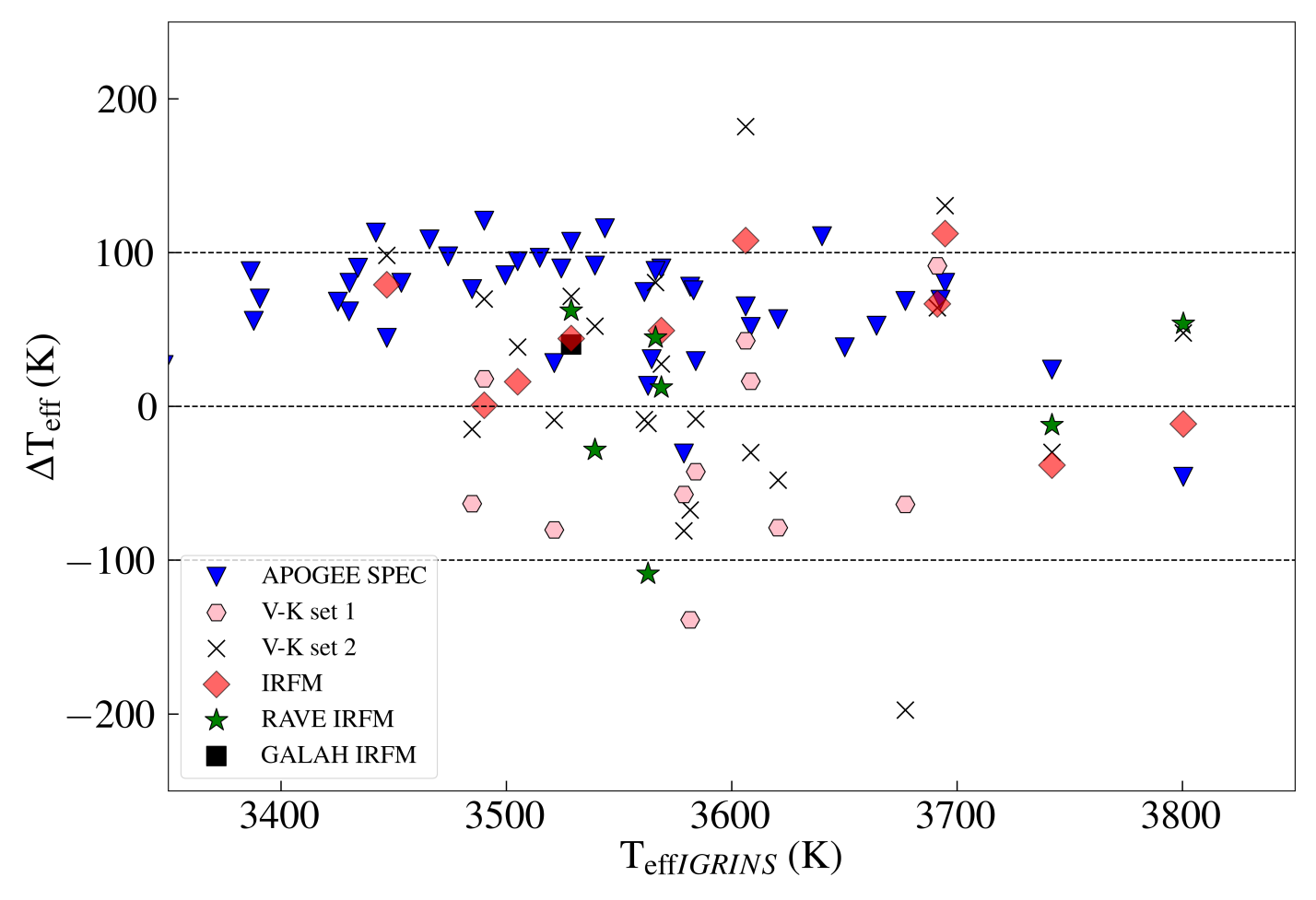


Fig. 5. Differences (GALAH, RAVE, APOGEE, (V–K), IRFM – our method) in $T_{\rm eff}$ as a function of the $T_{\rm eff}$ derived using our method on the x-axis. The dashed black lines indicate the difference values of $-100 \, \text{K}$, $0 \, \text{K}$, and $+100 \, \text{K}$. Differently colored symbols represent the values from different sources: Inverted blue triangles show APOGEE spectroscopic estimates, black squares show GALAH IRFM estimates, green stars show RAVE IRFM estimates, red diamonds show our IRFM $T_{\rm eff}$ estimates, and pink hexagons show $T_{\rm eff}$ estimated using the $T_{\rm eff}$ vs. (V–K) relation from Bessell et al. (1998) with extinctions in V and K based on the E(B-V) values from APOGEE.

available in the literature. In particular, the scatter with respect to several photometric determinations shows the uncertainty that is introduced by the limited precision to which reddening can be estimated. Because our determined effective temperatures agree excellently with the six nearby well-studied M giants in the IGRINS spectral library (in Fig. 3), our values are very probably more accurate. Especially the moderately tight offset against $T_{\rm eff}$ from APOGEE indicates a good internal precision.

5.2. Uncertainties in the derived stellar parameters

As explained in Sect. 4, our method for estimating stellar parameters largely depends on the oxygen abundance, which we fixed based on the metallicity of the star and the Milky Way population to which the star belongs (see Fig. 1). Thus, the assumption of the population or the oxygen abundance may be considered the main source of uncertainty for our stellar parameters. Hence, in order to estimate typical uncertainties in the parameters and abundances we derived, we implemented our method assuming that the 38 thin-disk stars in the solar neighborhood sample are thick-disk stars and vice versa for the 6 thick-disk stars. This is similar to the misclassification of star 39 as a thin-disk star in Sect. 5.1.2.

The results of this exercise are shown in Fig. 6. The differences in oxygen abundance are plotted on the x-axis, and the differences in the other six stellar parameters are plotted on the y-axis in each panel. In this figure, actual thick-disk stars have negative Δ [O/Fe] because [O/Fe] is lower for the thin-disk trend, and the actual thin-disk stars have positive Δ [O/Fe]. When a lower oxygen abundance is assumed for the most metal poor star, star 10, the stellar parameters were outside our adopted grid limits. Hence, we omitted this star in this exercise. For the maximum difference of ±0.2 dex in [O/Fe], we found typical differences of $\pm 200 \,\mathrm{K}$ in T_{eff} , $\pm 0.25 \,\mathrm{dex}$ in $\log g$, $\pm 0.2 \,\mathrm{km \, s^{-1}}$ in ξ_{micro} , $\pm 0.2 \, \text{dex}$ in [C/Fe], and $\pm 0.2 \, \text{dex}$ in [N/Fe]. The difference in metallicity is found to be closer to 0 for [O/Fe] differences of +0.2 and -0.2 dex, but larger (up to $\sim +0.2$ dex) in the range $0.0 < \Delta [O/Fe] < 0.2$ dex. Thus, assuming a typical uncertainty of 0.15 dex in [O/Fe], the parameters we estimated using our method have typical uncertainties of ± 100 K in $T_{\rm eff}$, ± 0.2 dex in $\log g$, ± 0.1 dex in [Fe/H], ± 0.1 km s⁻¹ in ξ_{micro} , ± 0.1 dex in [C/Fe], and ±0.1 dex in [N/Fe]. Again, as we demonstrated for star 39 in Sect. 5.1.2, however, an incorrect classification would be caught in the derived alpha abundances, and a corrective iteration can be run. To ensure this was not a chance occurrence, we determined [Mg/Fe] for all stars using the stellar

Table 3. Stellar parameters and [C/Fe] and [N/Fe] values of each star, along with their assumed stellar population and [O/Fe] based on the APOGEE [Mg/Fe] vs. [Fe/H] trend.

Index	Population	T _{eff}	$\log g \\ \log(\text{cm s}^{-2})$	[Fe/H] dex	$\xi_{\rm micro}$ km s ⁻¹	[C/Fe] dex	[N/Fe] dex	[O/Fe] dex	Cross match
1	41. :	3490		-0.28					
1	thin thin	3694	0.48 0.74	-0.28 -0.45	2.03 1.88	-0.02 0.02	0.17 0.19	0.1 0.16	_
2 3	thick	3562	0.74	-0.43 -0.51	2.14	0.02	0.19	0.10	RAVE
4	thick	3742	1.08	-0.31	1.78	0.21	0.3	0.38	RAVE
5	thin	3677	0.92	-0.07	1.78	-0.12	0.29	0.13	
6	thin	3692	0.92	-0.07 -0.54	2.01	0.02	0.21	0.04	
7	thin	3583	0.08	-0.54 -0.66	2.39	0.02	0.31	0.19	_
8	thick	3620	0.42	-0.38	2.39	0.03	0.33	0.24	
9	thin	3608	0.65	-0.58 -0.52	2.1	0.17	0.22	0.33	_
10	thick	3800	0.59	-0.32 -0.92	2.72	0.00	0.27	0.19	RAVE
11	thin	3521	0.39	-0.52	2.72	0.21	0.37	0.30	KAVE -
12	thin	3484	0.32	-0.52 -0.55	2.19	0.04	0.31	0.13	_
13	thin	3581	0.52	-0.33 -0.21	2.15	-0.09	0.31	0.2	_
14	thin	3606	0.52	-0.56	1.96	0.04	0.27	0.2	
15	thin	3561	0.56	-0.36	2.24	-0.08	0.41	0.13	
16	thin	3568	0.96	0.25	1.83	-0.18	0.39	-0.08	RAVE, GALAH (*)
17	thin	3566	0.51	-0.46	2.02	0.16	0.24	0.16	RAVE
18	thin	3539	0.5	-0.41	2.05	0.03	0.23	0.15	RAVE, GALAH (*)
19	thin	3528	0.61	-0.41 -0.15	1.92	-0.02	0.23	0.15	RAVE, GALAH
20	thin	3504	0.61	-0.08	1.81	0.02	0.16	0.03	-
21	thin	3474	0.69	0.12	1.94	-0.07	0.10	-0.04	_
22	thin	3543	0.8	0.12	1.95	-0.05	0.21	-0.04	_
23	thin	3386	0.55	0.11	1.82	-0.04	0.14	-0.05	_
24	thin	3387	0.52	0.08	1.92	-0.03	0.21	-0.03	_
25	thin	3453	0.63	0.08	1.91	-0.1	0.22	-0.03	_
26	thin	3465	0.62	0.04	1.83	-0.09	0.33	-0.02	_
27	thin	3430	0.54	0.0	1.95	-0.02	0.16	-0.0	_
28	thin	3499	0.62	-0.06	2.01	-0.07	0.25	0.02	_
29	thin	3639	0.89	-0.0	1.76	-0.05	0.08	0.01	_
30	thin	3524	0.56	-0.25	1.98	0.02	0.15	0.09	_
31	thin	3664	1.11	0.23	1.99	-0.09	0.35	-0.08	_
32	thin	3430	0.55	0.02	1.92	-0.09	0.21	-0.01	_
33	thin	3425	0.54	0.02	1.87	-0.07	0.25	-0.01	_
34	thin	3442	0.68	0.18	1.85	-0.0	0.16	-0.06	_
35	thin	3514	0.53	-0.26	2.02	-0.04	0.16	0.09	_
36	thin	3446	0.61	0.08	1.99	-0.04	0.21	-0.03	_
37	thin	3650	0.98	0.1	1.8	-0.11	0.29	-0.04	_
38	thin	3582	0.96	0.23	1.8	-0.11	0.31	-0.09	_
39	thick	3691	0.76	-0.4	1.98	0.17	0.14	0.34	_
40	thin	3564	0.95	0.25	2.2	-0.04	0.38	-0.09	_
41	thin	3347	0.46	0.09	1.98	-0.09	0.21	-0.03	_
42	thin	3390	0.48	0.01	1.96	-0.01	0.27	-0.0	_
43	thin	3434	0.59	0.07	1.93	-0.07	0.24	-0.02	_
44	thick	3578	0.45	-0.59	2.26	0.08	0.54	0.41	GALAH (*)

Notes. (*)No IRFM T_{eff} in GALAH DR3.

parameters determined based on a misclassification. We found that the [Mg/Fe] abundances decrease further for the incorrectly classified thin-disk star and it increases further for the incorrectly classified thick-disk star. This is demonstrated in Fig. 7. We are therefore safely be able to catch any misclassification of a highor low-alpha star by inspecting the derived [Mg/Fe] ratio.

Another source of uncertainty is the use of 10 Gyr YY isochrone to constrain $\log g$. As discussed in Rich et al. (2017), different age tracks for giants overlap, which in turn should result

in a negligible difference in $\log g$ when we choose a lower age isochrone track. We find that $\log g$ increases by only $\sim 0.1\,\mathrm{dex}$ when we use a $2\,\mathrm{Gyr}$ YY isochrone instead of the $10\,\mathrm{Gyr}$ isochrone.

Thus, we estimated the uncertainties in the derived stellar parameters using our method to be $\pm 100\,\mathrm{K}$ in T_{eff} , $\pm 0.2\,\mathrm{dex}$ in $\log g$, $\pm 0.1\,\mathrm{dex}$ in [Fe/H], and $\pm 0.1\,\mathrm{km\,s^{-1}}$ in ξ_{micro} . Within these uncertainties, our parameters are in line with the comparison samples and methods presented in Figs. 3–5.

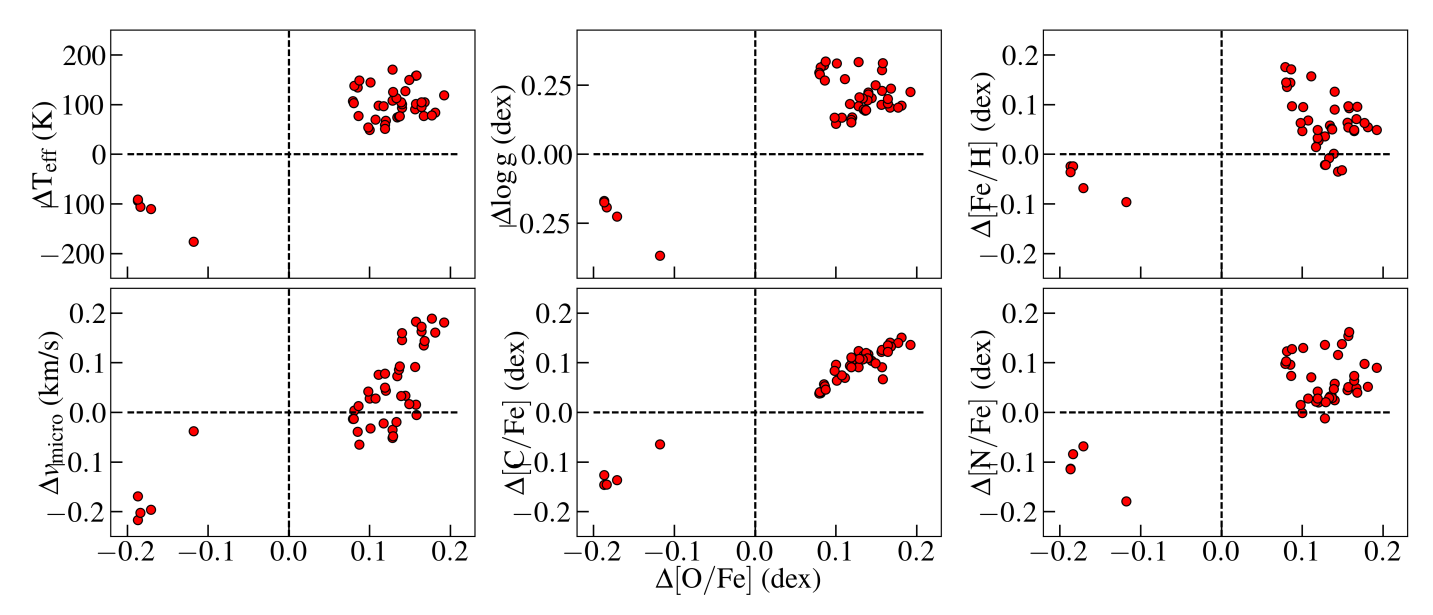


Fig. 6. Difference in T_{eff} , log g, [Fe/H], ξ_{micro} , [C/Fe], and [N/Fe] as a function of the difference in [O/Fe] resulting from the changed population assumption from thin to thick disk and vice versa for the 44 solar neighborhood M giants. Circles with positive δ [O/Fe] values represent thin-disk stars that were assumed to be thick-disk stars for this exercise.

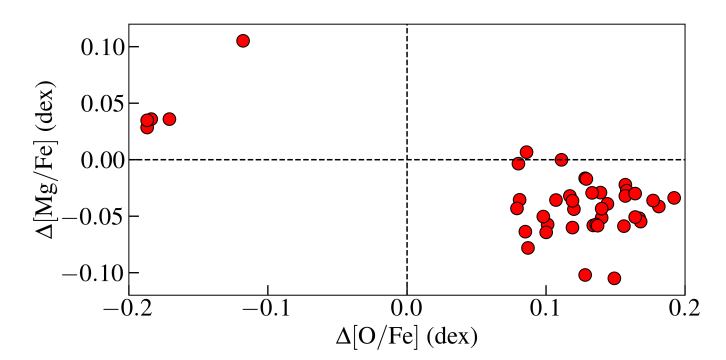


Fig. 7. Same as Fig. 6, but for the difference in [Mg/Fe] plotted on the *y*-axis.

6. α -abundance trends

Based on the stellar parameters determined using our iterative method, we determined the elemental abundances of the following α elements: Mg, Si, Ca, and Ti, for the 6 nearby M giants and 44 solar neighborhood M giants. We adopted the solar abundance values for Mg (A(Mg) $_{\odot}$ = 7.53), Si (A(Si) $_{\odot}$ = 7.51), Ca (A(Ca) $_{\odot}$ = 6.31), and Ti (A(Ti) $_{\odot}$ = 4.90) from Grevesse et al. (2007). In the following subsections, we discuss the individual and mean elemental abundance trends determined from a selected set of absorption lines of each element in the H and K bands. For each element, we fit the selected lines individually and determined the mean abundance value after removing lines that were too noisy, affected by spurious features, or affected by telluric lines that were not eliminated well enough in the telluric-line removal procedure. From these chosen abundance sets, we determined the mean abundance and a line-byline scatter of each element for every star (see Tables A.6–A.9). We also compared the mean elemental abundance trends to the optical solar neighborhood trends from the GILD sample and to the APOGEE DR17 spectroscopic values if available. This comparison also serves as a way to further validate our stellar parameters and hence the method we used to determine them.

In addition to the line-by-line scatter reported in Tables A.6-A.9, we determined the uncertainties in the elemental abundance estimates from each line that arise from the uncertainties in stellar parameters. As mentioned in Sect. 5.2, the parameters estimated using our method have typical uncertainties of $\pm 100 \,\mathrm{K}$ in $T_{\rm eff}$, $\pm 0.2 \,\mathrm{dex}$ in $\log g$, ± 0.1 dex in [Fe/H], and ± 0.1 km s⁻¹ in ξ_{micro} . We selected seven stars with metallicities of ~ -0.9 dex (star 10), -0.5 dex (stars 11 and 44), -0.25 dex (star 30), 0.0 dex (star 29), 0.1 dex (star 41), and 0.25 dex (star 40) to determine the uncertainties. Thus we covered the entire metallicity range we explored in this study. We randomly generated 50 sets of stellar parameters following a normal distribution, with the stellar parameter value as the mean and these typical uncertainties as the standard deviation, and we reanalyzed each stellar spectrum using these parameters. We generated 50 sets of parameters for each of the seven stars. The resulting distribution of the estimated abundances from each line was fit with a Gaussian function. The dispersion estimated from this fit gives the uncertainty in abundances. Table A.10 lists the uncertainties from the individual elemental lines as well as the mean uncertainty corresponding to each elemental abundance for these seven stars. The mean abundance uncertainties range from 0.04–0.08 dex for [Mg/Fe], 0.07–0.11 dex for [Si/Fe], 0.04–0.07 dex for [Ca/Fe], and 0.06–0.11 dex for [Ti/Fe].

6.1. Magnesium

We determined the magnesium abundances from three lines in the K band: 21059.76 Å, 21060.89 Å, and 21458.87 Å. The two H-band Mg I lines at 15740.70 Å and 15748.89 Å could not be used because these two lines were saturated based on their insensitivity to a ± 0.2 dex variation in Mg abundances. In addition, the Mg abundances from these two lines are found to have a strong correlation with the microturbulence $(0.1-0.2 \, \text{dex})$ variation for $\Delta \xi_{\text{micro}} = \pm 0.2 \, \text{dex}$.

In Fig. 8 we plot the selected Mg lines in the observed spectra of one thin-disk star (star 40, top row panels) and one thick-disk star (star 44, bottom row panels), the synthetic spectrum fit to these line, and the variation in the fit resulting in a

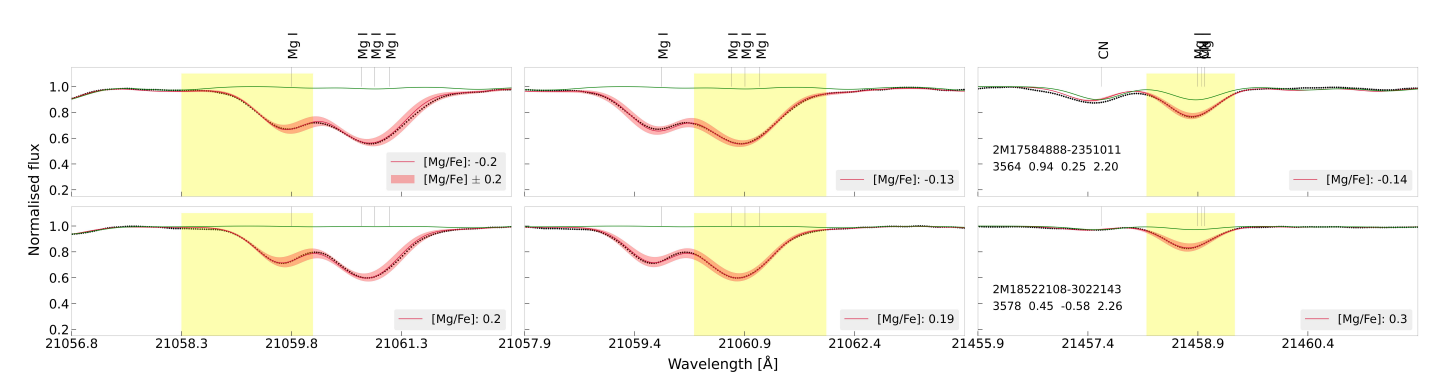


Fig. 8. Wavelength regions centered at the five selected magnesium lines for the thin-disk star 2M17584888-2351011 (star 40; top row panels) and the thick-disk star 2M18522108-3022143 (star 44; bottom row panels). The panels in each row are arranged in increasing order of the wavelengths of the selected lines. In each panel, the black circles denote the observed spectrum, the crimson line denotes the best-fit synthetic spectrum, and the red band denotes the variation in the synthetic spectrum for a difference of ± 0.2 dex in the [Mg/Fe]. The yellow bands in each panel represent the line masks defined for the Mg lines, wherein SME fits observed spectra by varying the magnesium abundance and finds the best synthetic spectra fit by ξ^2 minimization. The green line shows the synthetic spectrum without Mg, also indicating any possible blends in the line. The [Mg/Fe] values corresponding to the best-fit case for each Mg line are listed in each panel. All identified atomic and molecular lines are also denoted in the top part of the top row panels.

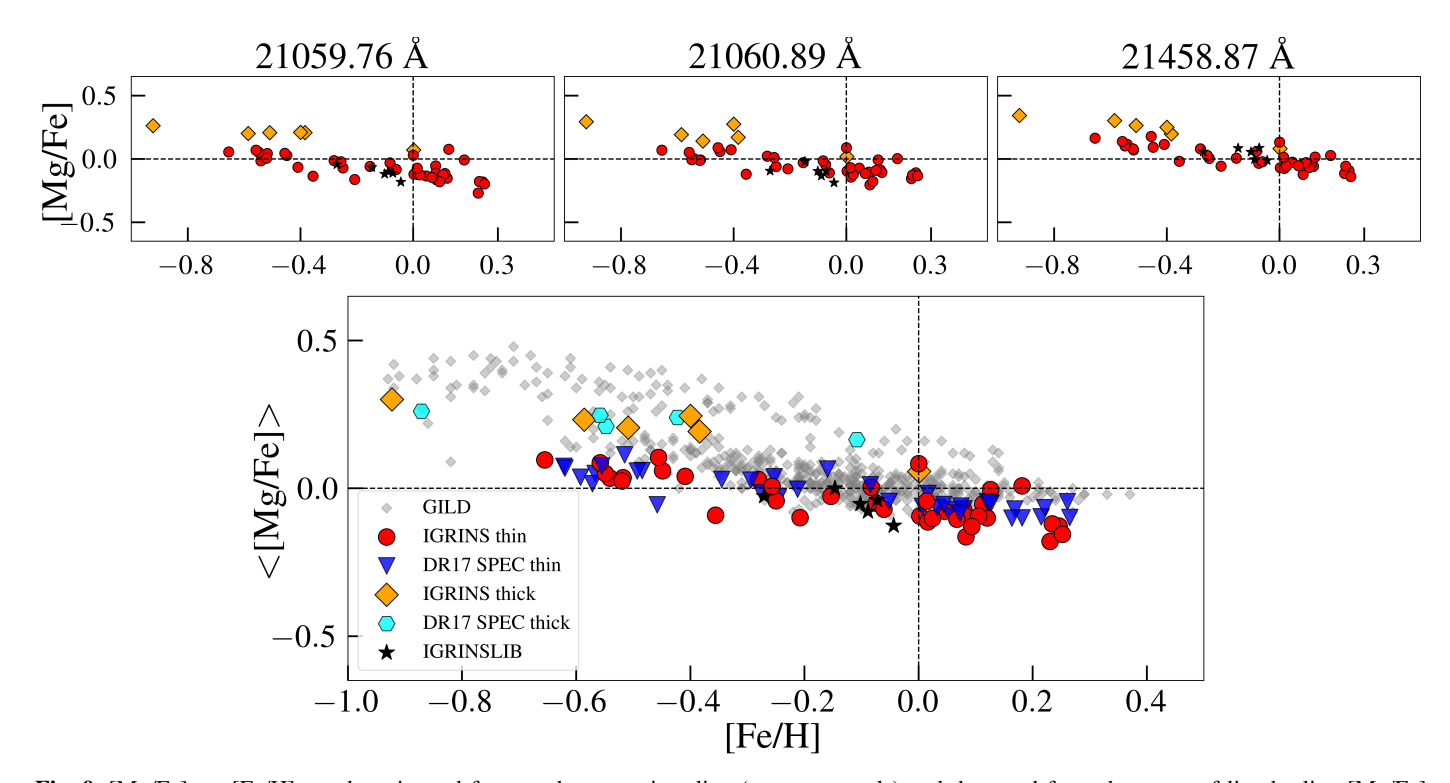


Fig. 9. [Mg/Fe] vs. [Fe/H] trends estimated from each magnesium line (top row panels) and the trend from the mean of line-by-line [Mg/Fe] estimates (bottom panel). The red circles, orange diamonds, and black stars in all panels represent the 38 thin-disk solar neighborhood M giants, six thick-disk solar neighborhood M giants and the six nearby M giants, respectively. The gray diamonds in the bottom panel represent the stars in the GILD sample, with the parameters and abundances estimated from optical FIES spectra and shifted down by 0.1 dex. The inverted blue triangles (thin-disk) and cyan hexagons (thick-disk) represent the APOGEE spectroscopic estimates for the 43 solar neighborhood stars.

change of $\pm 0.2\, dex$ in the abundance value. We also show the line masks defined for the Mg lines (avoiding the neighboring lines) wherein the SME fits the observed spectra by varying the magnesium abundance and finds the best synthetic spectra fit by chi-square minimization. We also plot the synthetic spectrum without Mg, indicating any possible blends in the line. The stellar parameters estimated for each star are listed in the leftmost panels along with the derived abundance from each line in the corresponding panel.

We plot the Mg abundance trend ([Mg/Fe] versus [Fe/H]) from each of these lines in the top five panels and the mean Mg

abundance trend in the bottom panel of Fig. 9. In these plots, the red circles (thin disk) and orange diamonds (thick disk) represent the solar neighborhood sample, and black stars represent the six nearby M giants. In the bottom panel, the GILD Mg abundance trend is plotted as gray diamonds, and the APOGEE spectroscopic Mg values for the 43 solar neighborhood stars (except for star 39) are plotted as inverted blue triangles (thin disk) and cyan hexagons (thick disk).

This is also evident in the negligible variation in the synthetic spectrum fit to the two H-band lines for the ± 0.2 dex [Mg/Fe] variation in Fig. 8. The [Mg/Fe] trend from all three K-band

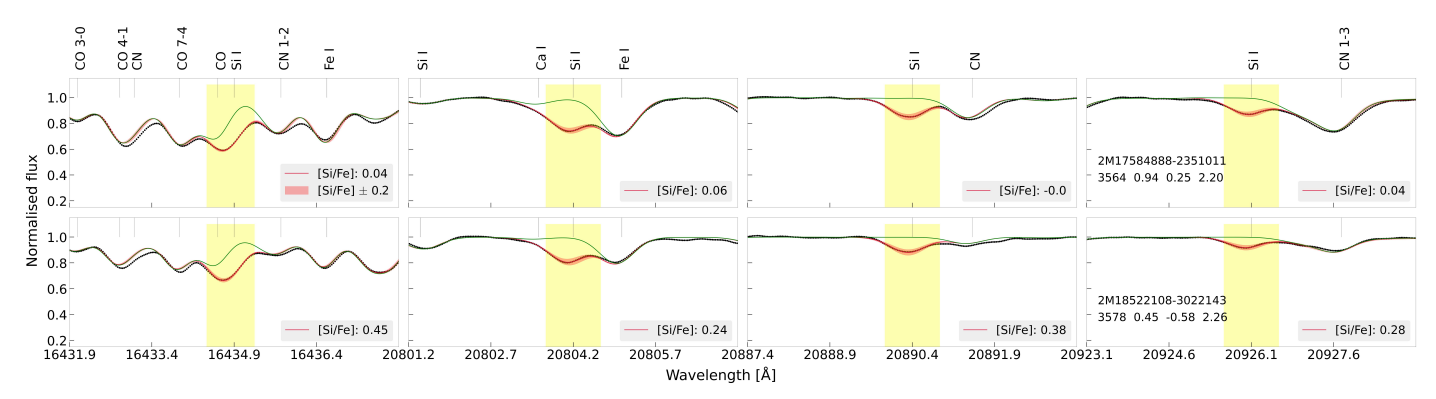


Fig. 10. Similar to Fig. 8, but for the silicon lines.

lines shows a decreasing trend with increasing metallcity, especially at supersolar metallicities (as expected from chemical evolution models; see Matteucci 2021) and a clear enhancement in [Mg/Fe] for thick-disk stars compared to thin-disk stars. [Mg/Fe] values from the multiplet lines 21059.76 Å and 21060.89 Å are found to have subsolar [Mg/Fe] at solar metallicity, unlike those from the 21458.87 Å that pass through the solar value, as expected. This line also has a comparatively accurate qf value, as listed in NIST database with an accuracy grade of B+ (which means $\leq 7\%$). The line parameters we used for the two multiplet K-band lines were found to result in a good synthetic spectrum fit to the lines in the high-resolution solar and Arcturus spectra. Nieuwmunster et al. (2023) used the same lines and line data and found a similar low trend for inner bulge stars and warmer solar neighborhood K giants. We would also like to point out that the [Mg/Fe] values determined from each line for the six near by M giants are consistent with the corresponding trend obtained for the solar neighborhood stars.

We determined the mean [Mg/Fe] for each star from the lines that were deemed to have a good synthetic spectrum fit by visual check and were not affected by noise or telluric lines. The individual and mean [Mg/Fe] for each star along with the standard deviation value is listed in Table A.6. Our mean [Mg/Fe] trend shows a clear dichotomy of the thin and thick disk, with enhanced values for thick-disk stars. In the comparison with the APOGEE DR17 spectroscopic [Mg/Fe] values for the same stars, our mean abundances for thick- and thin-disk stars are consistent with the APOGEE values. The APOGEE [Mg/Fe] trends and our trends pass through subsolar [Mg/Fe] at solar metallicity. The [Mg/Fe] trend for warmer stars in the GILD sample passes through supersolar [Mg/Fe] values at solar metallicities with a systematic difference of $\sim 0.1-0.2$ dex with respect to our [Mg/Fe] trend. In Fig. 9 we therefore shifted the GILD trend down by 0.1 dex in order to normalize this comparison sample to the solar value for better comparison. The LTE [Mg/Fe] values for our stars agree well with the original GILD trend (see Sect. 6.5). The systematic difference between our trend and the GILD trend might be caused by the use of NLTE grids in this work and LTE values in GILD.

6.2. Silicon

We determined [Si/Fe] for the stars in the nearby M giant sample and the solar neighborhood sample from one line at 16434.93 Å in the H band and three lines in the K band: 20804.20 Å, 20890.37 Å, and 20926.14 Å. In Fig. 10, we plot the synthetic spectrum fits to these lines in the observed spectra of one thindisk star (top panels) and one thick-disk star (bottom panels). In

Fig. 11 we plot our individual [Si/Fe] trends (top panels) and the mean [Si/Fe] (bottom panel) along with [Si/Fe] from the GILD sample and APOGEE DR17.

The synthetic spectrum fit to all four lines for the sample of thin- and thick-disk stars in Fig. 10 is reasonably good. The mean [Si/Fe] is higher for all six thick-disk stars. Only one good Si line is available for the solar metallicity thick-disk star, star 4 ([Fe/H] = 0.0), from which we determined a high [Si/Fe] value of ~0.18 dex. This might be the reason for the distinctly high [Si/Fe] but lower abundance values of other alpha elements for this star. The mean thin-disk trend of the solar neighborhood and nearby M giant sample is consistent with the GILD sample thin-disk trend at all metallicities, but we find an enhancement of $\sim 0.05-0.1$ dex in our thick-disk trend compared to the GILD thick-disk trend. A similar difference is seen with respect to the APOGEE [Si/Fe] abundances of thick-disk stars and also compared to the [Fe/H] < -0.5 thin-disk stars. Overall, the thin-disk trend shows a small scatter, and the thick-disk trend is clearly higher in [Si/Fe].

6.3. Calcium

We used five calcium absorption lines to determine [Ca/Fe], three in the *H* band, 16150.76 Å, 16155.24 Å, and 16157.36 Å, and two in the *K* band, 20962.57 Åand 20972.53 Å. In Fig. 12, we plot the synthetic spectrum fits to these lines in the observed spectra of one thin-disk star (top panels) and one thick-disk star (bottom panels). In Fig. 13 we plot our individual [Ca/Fe] trends (top panels) and the mean [Ca/Fe] (bottom panel) along with [Ca/Fe] from the GILD sample and APOGEE DR17.

As shown in Fig. 12, we were able to fit all five lines very well. In addition, these lines strongly depend on the Ca abundance, as indicated by the significant variation in the synthetic spectrum. The variation of ±0.2 dex in [Ca/Fe]. The [Ca/Fe] trends from all six lines follows a downward trend, although with a shallower slope than for [Mg/Fe], for example. Above solar metallicity, [Ca/Fe] seems to at least level off, to decrease again at [Fe/H] > 0.2 dex. A larger sample would clarify this observation. The mean [Ca/Fe] values follow the same trend, and the five metal-poor thick-disk stars have higher mean abundances than the thin-disk stars. No similar enhancement is detected for the solar metallicity thick-disk star. Unlike for Mg and Si, there is no clear separation between the thin- and thick-disk stars in the [Ca/Fe] trend from the GILD sample. Compared to the GILD trend, our mean [Ca/Fe] trend is systematically lower by 0.05 dex, but passes through solar [Ca/Fe] at solar metallicity. Similar to Mg, we therefore shifted the GILD trend down by

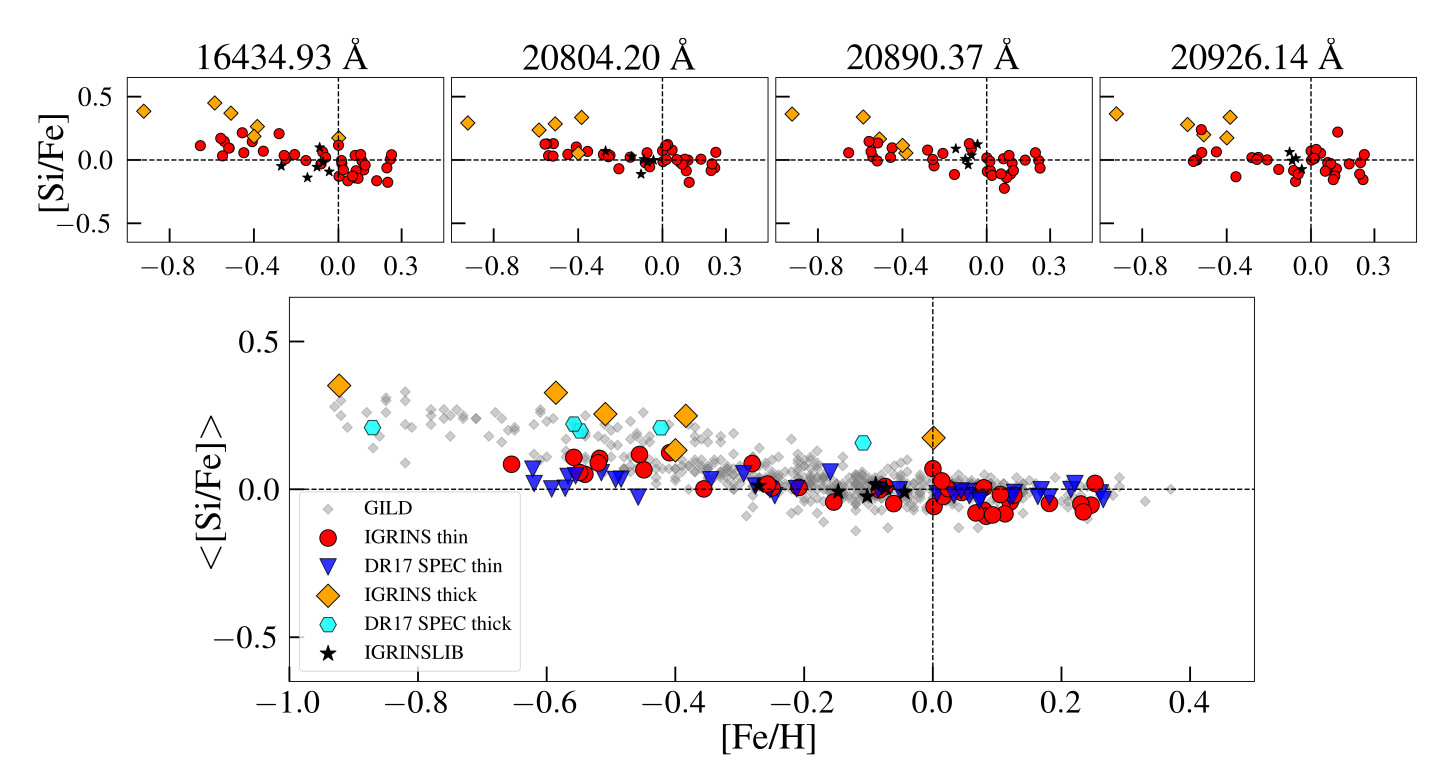


Fig. 11. Similar to Fig. 9, but for [Si/Fe].

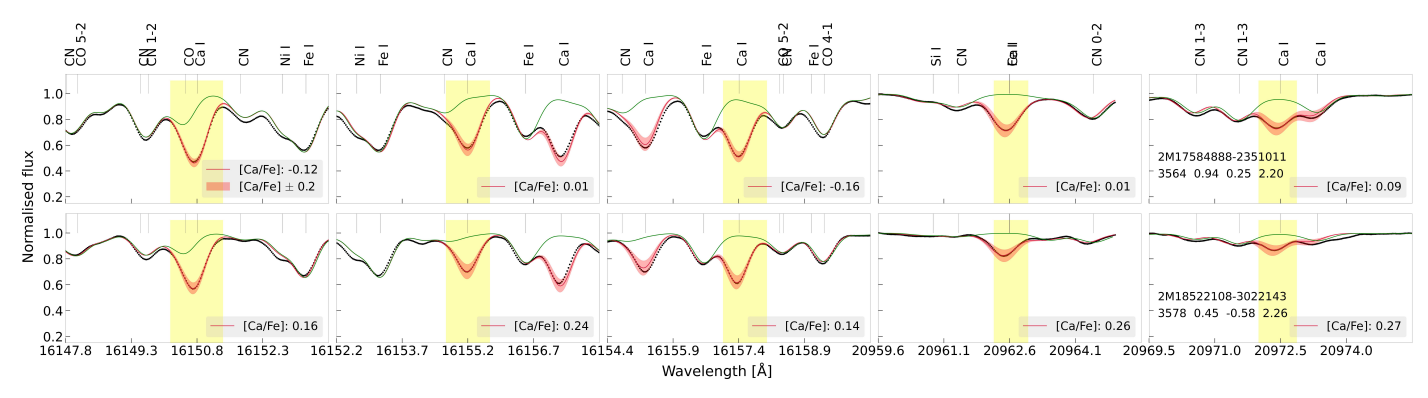


Fig. 12. Similar to Fig. 8, but for calcium lines.

0.05 dex in order to normalize this comparison sample to the solar value to allow for a better comparison. The [Ca/Fe] trend from APOGEE DR17 sample follows a downward trend that continues to decrease at higher metallicities. The DR17 [Ca/Fe] values are lower for the thick-disk stars and thus do not show any clear separation with respect to the thin-disk stars.

6.4. Titanium

Only two lines were used to determine [Ti/Fe]. One line in the H band, 16330.54 Å, and one line in the K band, 21149.62 Å. In Fig. 14, we plot the synthetic spectrum fits to these lines in the observed spectra of one thin-disk star (top panels) and one thick-disk star (bottom panels). In Fig. 15 we plot our individual [Ti/Fe] trends (top panels) and the mean [Ti/Fe] (bottom panel) along with [Ti/Fe] from the GILD sample and APOGEE DR17.

Compared to the *H*-band line at 16330.54 Å, the *K*-band line at 21149.62 Å is weaker and blended with CN ($\nu = 1-3$). The [Ti/Fe] trend determined using the line at 16330.54 Å is found to have lower scatter at subsolar metallicities than the trend determined from the line at 21149.62 Å. This may be attributed to the CN (v = 1-3) blend in the left wing of the K-band line, as shown in Fig. 14. This scatter is carried forward to the mean [Ti/Fe] trend for low-metallicity stars ($[Fe/H] < -0.4 \, dex$). The metal-poor thick-disk stars show a clear enhancement compared to the thin-disk stars, however. Furthermore, the mean [Ti/Fe] abundance trend is consistent with the optical [Ti/Fe] trend from the GILD sample. Unfortunately, APOGEE DR17 does not provide [Ti/Fe] measurements for the 44 stars. The Ti I lines in the APOGEE wavelength regime (H band) are very sensitive to T_{eff} (Jönsson et al. 2018, 2020). Hence, it is reassuring for our method and especially for our determined $T_{\rm eff}$ that the [Ti/Fe] determined using

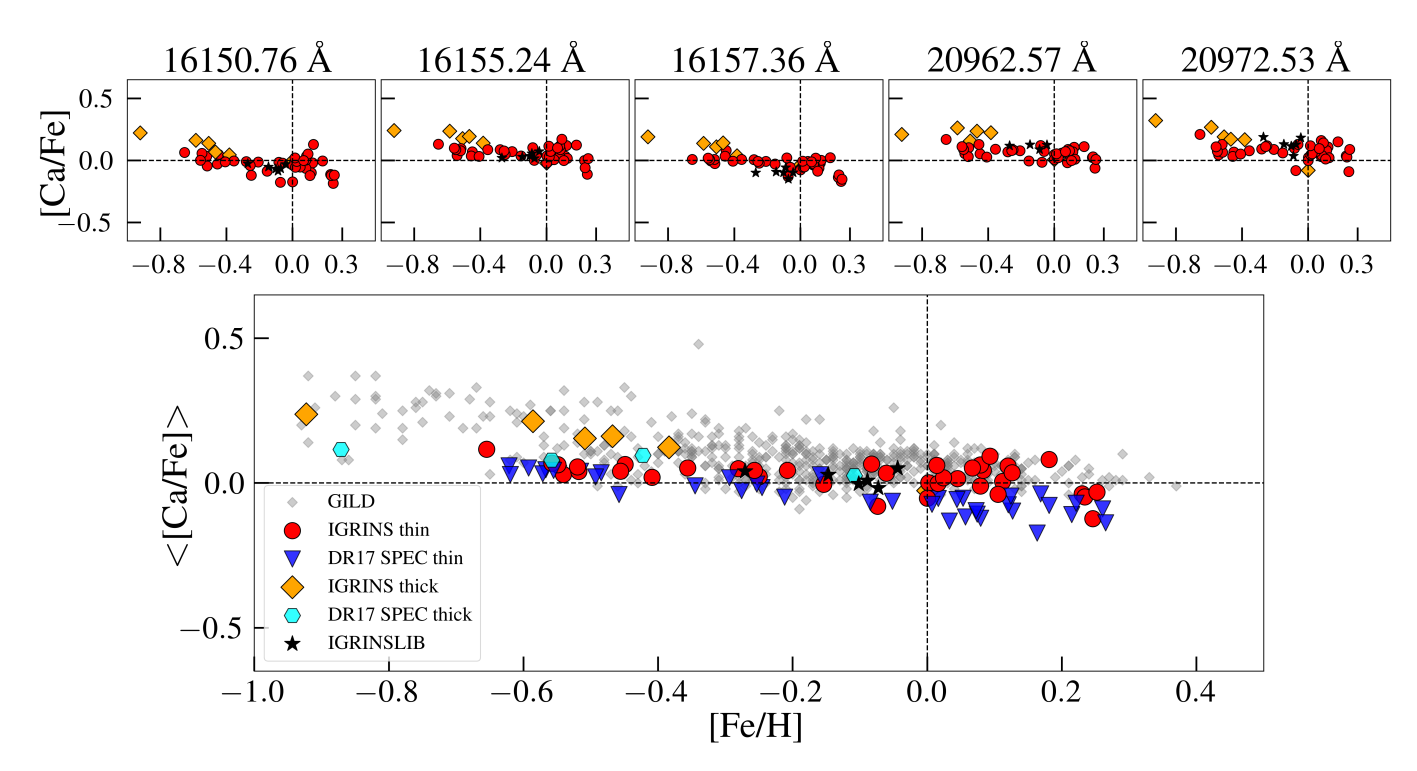


Fig. 13. Similar to Fig. 9, but for [Ca/Fe]. The GILD [Ca/Fe] have been shifted down by 0.05 dex to normalize the comparison sample to the solar value.

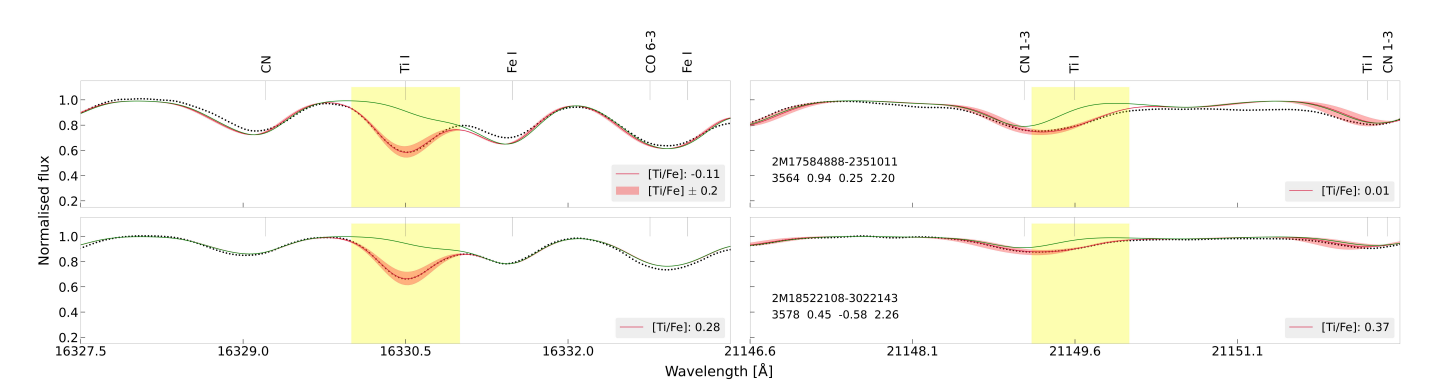


Fig. 14. Similar to Fig. 8, but for the titanium lines.

our stellar parameters is consistent with the trend from the optical spectra.

6.5. LTE and non-LTE comparison

As mentioned in Sect. 3, we applied NLTE corrections to the abundance measurements of Mg, Si, and Ca. In addition, we estimated the abundances for all three elements without applying NLTE corrections. Figure 16 shows the NLTE (brown) and LTE trends (cyan) for all three elements as a function of [Fe/H]. The NLTE-LTE difference for [Mg/Fe] and [Ca/Fe] ranges from -0.05 to -0.15 dex, and there is no significant NLTE-LTE difference for [Si/Fe]. This means that when NLTE corrections are applied, the abundance values for Mg and Si become lower.

7. Conclusions

For abundance studies, a general method for determining the important stellar parameters for M giants is needed. For exam-

ple, in order to study stellar abundances and the chemical evolution of stellar populations in dust-obscured regions, such as the inner bulge and Galactic center region, the intrinsically bright M giants observed in the NIR are an optimal option. Not only is the extinction lower in the infrared, but cool stars, such as M giants, can only be analyzed in the NIR due to the ubiquitous TiO features in optical spectra of stars with $T_{\rm eff} < 4000$ K. Because of the uncertainties in photometric methods, a method for determining the stellar parameters for M giants from the NIR spectra themselves is needed. This method would allow these regions to be analyzed efficiently.

In this quest to determine reliable stellar parameters and elemental abundances of M giant stars from their NIR spectra, we therefore developed an iterative method that was tested for $3400 \lesssim T_{\rm eff} \lesssim 4000$ K and that we presented here. We used high-resolution ($R \sim 45\,000$) spectra in the H band that were observed with the IGRINS spectrometer. IGRINS spectra cover the entire wavelength range of the H and K bands ($\sim 14\,000\,\text{Å}$) to $25\,000\,\text{Å}$), which provides a wealth of spectral lines also for the subsequent study of stellar abundances.

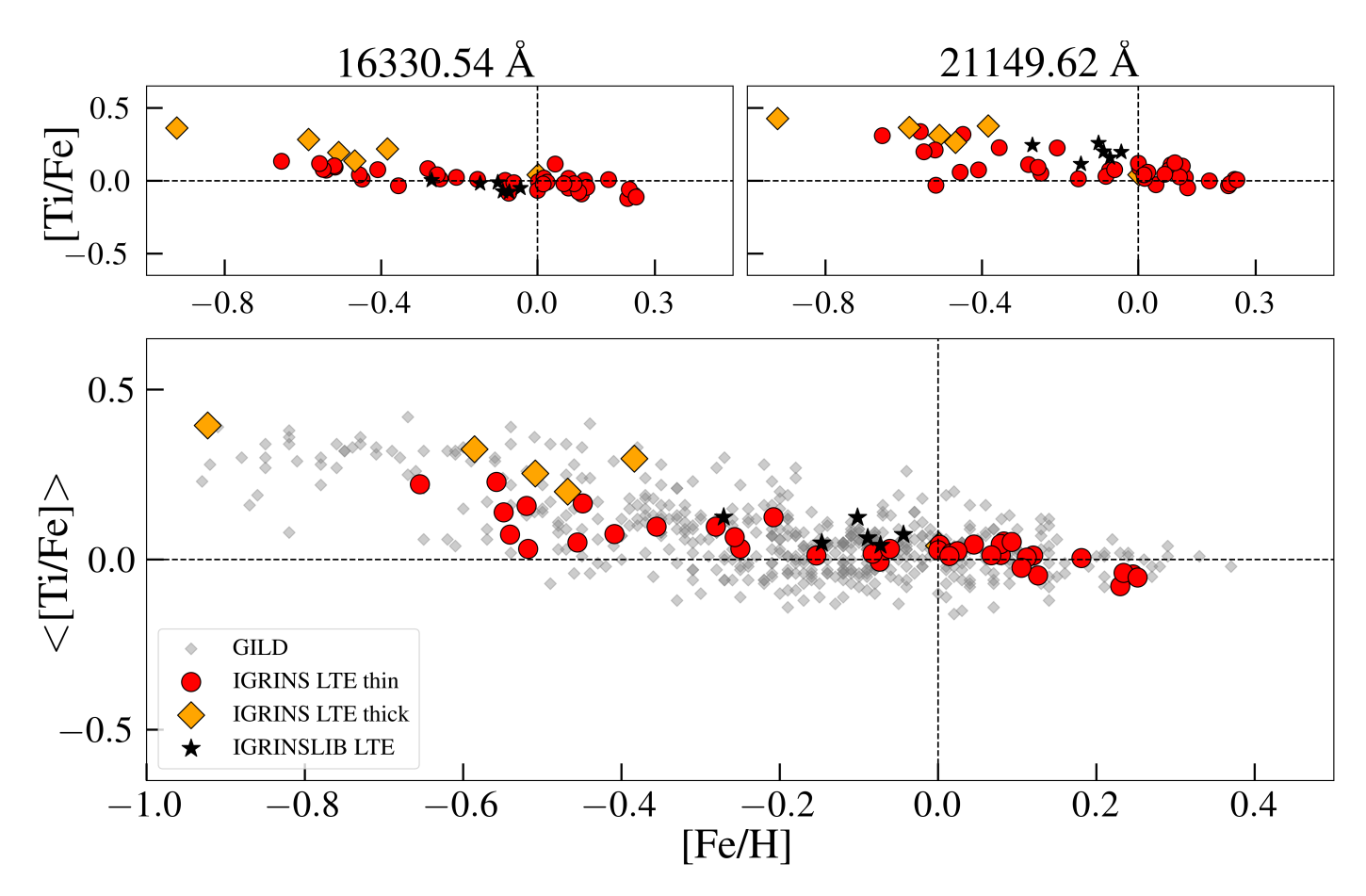


Fig. 15. Similar to Fig. 9, but for [Ti/Fe].

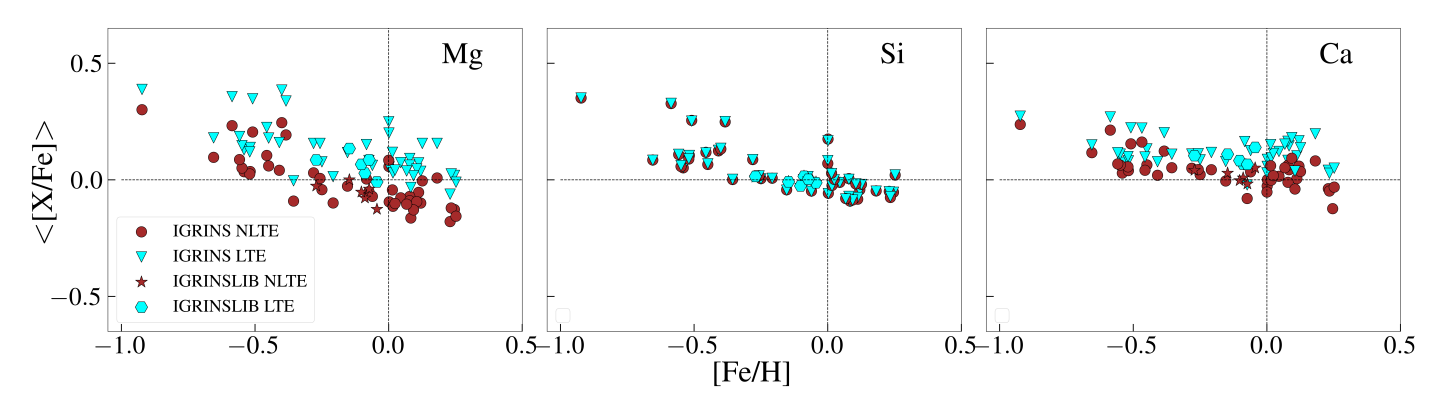


Fig. 16. NLTE (brown) and LTE (cyan) abundance trends as a function of [Fe/H] for [Mg/Fe], [Si/Fe], and [Ca/Fe] estimated for 44 solar neighborhood M giants (circles show NLTE and inverted triangle shows LTE) and six nearby M giants (stars show NLTE and hexagon show LTE). The difference between NLTE and LTE measurements for Si is negligible, and Mg and Ca show differences of 0.05–0.15 dex.

Because $T_{\rm eff}$ is one of the most crucial fundamental stellar parameters, we started by identifying ~15–20 $T_{\rm eff}$ sensitive molecular OH lines in the H band based on our investigations using the APOGEE M giant spectra and their parameters provided in the DR17 catalog. In addition to $T_{\rm eff}$, the OH line strengths also depend on the oxygen abundance, resulting in a degeneracy between $T_{\rm eff}$ and the oxygen abundance. We therefore fixed the oxygen abundance based on the metallicity of the star following the [O/Fe] versus [Fe/H] trend in Amarsi et al. (2019) for thin- and thick-disk stars (Fig. 1).

After the initial assumption of the stellar population, we started with an initial T_{eff} and [Fe/H] of 3500 K and 0.0 dex.

The $\log g$ value was chosen to be 0.65 dex from the 10 Gyr Yonsei-Yale (YY) isochrones, corresponding to the initially assumed $T_{\rm eff}$ and [Fe/H] by means of simple linear interpolation (Rich et al. 2017). Our method requires multiple iterations, wherein first, we determined $T_{\rm eff}$, [Fe/H], $\xi_{\rm micro}$, [C/Fe], and [N/Fe] using SME by fitting the selected set of OH, CN, CO, and Fe lines. We then determined $\log g$ based on the newly determined $T_{\rm eff}$ and [Fe/H] from the 10 Gyr YY isochrones. Similarly, the oxygen abundance was updated corresponding to the new [Fe/H]. With the updated $\log g$ and oxygen abundance, we determined new values of $T_{\rm eff}$, [Fe/H], $\xi_{\rm micro}$, [C/Fe], and [N/Fe], and this cycle was repeated until the differences between the

latest and previously determined values of all free parameters were negligible (Fig. 2). It is reassuring that even for an initial misidentification of the stellar population, this was able to be remedied by determining the [Mg/Fe] abundance, for instance. This clearly shows to which population the star belongs (see Sect. 5.2). Thus a final check of the assumed stellar population was made based on the determined α abundances, most importantly, the [Mg/Fe] abundance.

We validated our method by deriving the stellar parameters for six nearby well-studied M giants with spectra from the IGRINS spectral library. Furthermore, we demonstrated the accuracy and precision by determining the α -element trends versus metallicity for 44 solar neighborhood M giants from our two IGRINS runs on Gemini (we also included the six M giants in the α -element trends versus metallicity). Fortythree of the stars from our two IGRINS runs were also analyzed in APOGEE. The effective temperatures that we derived from our new method agree excellently well with the six nearby well-studied M giants (in Fig. 3), which indicates that the accuracy is indeed high. For the 43 solar neighborhood M giants, we find excellent agreement with APOGEE for T_{eff} , $\log g$, [Fe/H], ξ_{micro} , [C/Fe], [N/Fe], and [O/Fe], with mean differences and scatter (our method - APOGEE) of $-67\pm33 \text{ K}$, $-0.31\pm0.15 \text{ dex}$, $0.02\pm0.05 \text{ dex}$, $0.22\pm0.13 \text{ km s}^{-1}$, $-0.05\pm0.06\,\mathrm{dex}$, $0.06\pm0.06\,\mathrm{dex}$, and $0.02\pm0.09\,\mathrm{dex}$, respectively. Furthermore, the tight offset with a small dispersion compared to the APOGEE $T_{\rm eff}$ indicates a high precision in our derived temperatures and in those derived from the APOGEE pipeline (Fig. 5). The large scatter in the $T_{\rm eff}$ determined using photometric methods such as the IRFM and T_{eff} – (V – K) relations further emphasizes the necessity of developing spectroscopic methods like this to determine stellar parameters.

The typical uncertainties in the stellar parameters corresponding to ± 0.15 dex uncertainty in [O/Fe] are found to be ± 100 K in $T_{\rm eff}$, ± 0.2 dex in $\log g$, ± 0.1 dex in [Fe/H], ± 0.1 km s⁻¹ in $\xi_{\rm micro}$, ± 0.1 dex in [C/Fe], and ± 0.1 dex in [N/Fe]. Another source of uncertainty is the use of the 10 Gyr YY isochrone to constrain $\log g$. However, the difference in the derived surface gravity is smaller than 0.1 dex using a 2 Gyr YY isochrone instead of the 10 Gyr isochrone.

The α -element trends versus metallicity for Mg, Si, Ca, and Ti agree very well with the APOGEE DR17 trends for the same stars and with the GILD optical trends. The abundances for thick-disk stars are also clearly higher.

The two main limitations of our method are that the oxygen abundance is fixed and that theoretical isochrones are used to constrain $\log g$. We explored the effect of fixing incorrect oxygen abundances on the derived stellar parameters in detail and found ways to remedy these incorrect assumptions. To test the accuracy of the $\log g$ values we estimated from isochrones in our method, it is imperative to test our method on well-studied benchmark M giant stars (Heiter et al. 2015). We also need to increase the sample size of the solar neighborhood M giants to cover the full stellar parameter range, especially at temperatures lower than 3500 K.

As mentioned in Sect. 1, $T_{\rm eff}$ – line depth ratios (LDRs) relations have been proposed by many recent studies (Fukue et al. 2015; Taniguchi et al. 2018, 2021; Matsunaga et al. 2021; Afşar et al. 2023), especially in the NIR wavelength regimes (0.97–2.4 µm) for late-type giants with a broad range of $T_{\rm eff}$ s (3500–5400 K). Our method has only been tested on the cool stars ($T_{\rm eff}$ < 4000 K), and we need to apply our method on warmer stars with weaker molecular absorption lines in order to test its limits. The outcome from the LDR methods is limited to

 $T_{\rm eff}$ alone, however, while we determined the fundamental stellar parameters as well as the C and N abundances with our method.

To summarize, we have developed a method for determining reliable stellar parameters for M giants from their NIR spectra that can be made fully automatic for future NIR surveys.

Acknowledgements. We thank the anonymous referee for the constructive comments and suggestions that improved the quality and aesthetics of the paper. G.N. acknowledges the support from the Wenner-Gren Foundations and the Royal Physiographic Society in Lund through the Stiftelsen Walter Gyllenbergs fond. G.N. thanks Henrik Jönsson for enlightening discussions. N.R. acknowledges support from the Royal Physiographic Society in Lund through the Stiftelsen Walter Gyllenbergs fond and Märta och Erik Holmbergs donation and from Magnus Bergyalls stiffelse. This work used The Immersion Grating Infrared Spectrometer (IGRINS) was developed under a collaboration between the University of Texas at Austin and the Korea Astronomy and Space Science Institute (KASI) with the financial support of the US National Science Foundation under grants AST-1229522, AST-1702267 and AST-1908892, McDonald Observatory of the University of Texas at Austin, the Korean GMT Project of KASI, the Mt. Cuba Astronomical Foundation and Gemini Observatory. This work is based on observations obtained at the international Gemini Observatory, a program of NSF's NOIRLab, which is managed by the Association of Universities for Research in Astronomy (AURA) under a cooperative agreement with the National Science Foundation on behalf of the Gemini Observatory partnership: the National Science Foundation (United States), National Research Council (Canada), Agencia Nacional de Investigación y Desarrollo (Chile), Ministerio de Ciencia, Tecnología e Innovación (Argentina), Ministério da Ciência, Tecnologia, Inovações e Comunicações (Brazil), and Korea Astronomy and Space Science Institute (Republic of Korea). These results made use of the Lowell discovery Telescope (LDT) at Lowell Observatory. Lowell is a private, non-profit institution dedicated to astrophysical research and public appreciation of astronomy and operates the LDT in partnership with Boston University, the University of Maryland, the University of Toledo, Northern Arizona University and Yale University. This paper includes data taken at The McDonald Observatory of The University of Texas at Austin. The following software and programming languages made this research possible: TOPCAT (version 4.6; Taylor 2005); Python (version 3.8) and its packages ASTROPY (version 5.0; Astropy Collaboration 2022), SCIPY (Virtanen et al. 2020), MATPLOTLIB (Hunter 2007) and NUMPY (van der Walt et al. 2011).

References

```
Afşar, M., Bozkurt, Z., Topcu, G. B., et al. 2023, ApJ, 949, 86
Amarsi, A. M., Lind, K., Asplund, M., Barklem, P. S., & Collet, R. 2016,
   MNRAS, 463, 1518
Amarsi, A. M., Nordlander, T., Barklem, P. S., et al. 2018, A&A, 615, A139
Amarsi, A. M., Nissen, P. E., & Skúladóttir, Á. 2019, A&A, 630, A104
Amarsi, A. M., Lind, K., Osorio, Y., et al. 2020, A&A, 642, A62
Anstee, S. D., & O'Mara, B. J. 1991, MNRAS, 253, 549
Anstee, S. D., & O'Mara, B. J. 1995, MNRAS, 276, 859
Astropy Collaboration (Price-Whelan, A. M., et al.) 2022, ApJ, 935, 167
Baines, E. K., Thomas Armstrong, J., Clark, J. H., et al. 2021, AJ, 162, 198
Barklem, P. S., & O'Mara, B. J. 1997, MNRAS, 290, 102
Barklem, P. S., O'Mara, B. J., & Ross, J. E. 1998, MNRAS, 296, 1057
Bessell, M. S., & Brett, J. M. 1988, PASP, 100, 1134
Bessell, M. S., Castelli, F., & Plez, B. 1998, A&A, 333, 231
Biemont, E., Roland, G., Delbouille, L., & Brault, J. W. 1985, A&AS, 61,
Brault, J., & Noyes, R. 1983, ApJ, 269, L61
Brooke, J. S. A., Bernath, P. F., Western, C. M., et al. 2016, J. Quant. Spectr. Rad.
   Transf., 168, 142
Buder, S., Sharma, S., Kos, J., et al. 2021, MNRAS, 506, 150
Casagrande, L. 2008, Phys. Scr. Volume T, 133, 014020
Casagrande, L., & VandenBerg, D. A. 2014, MNRAS, 444, 392
Casagrande, L., Ramírez, I., Meléndez, J., Bessell, M., & Asplund, M. 2010,
   A&A, 512, A54
Casagrande, L., Wolf, C., Mackey, A. D., et al. 2019, MNRAS, 482, 2770
Casagrande, L., Lin, J., Rains, A. D., et al. 2021, MNRAS, 507, 2684
Civiš, S., Ferus, M., Chernov, V. E., & Zanozina, E. M. 2013, A&A, 554, A24
Cox, N. L. J., Cami, J., Kaper, L., et al. 2014, A&A, 569, A117
Demarque, P., Woo, J.-H., Kim, Y.-C., & Yi, S. K. 2004, ApJS, 155, 667 de Zeeuw, T., Tamai, R., & Liske, J. 2014, The Messenger, 158, 3
Ebenbichler, A., Postel, A., Przybilla, N., et al. 2022, A&A, 662, A81
Elyajouri, M., Lallement, R., Monreal-Ibero, A., Capitanio, L., & Cox, N. L. J.
   2017, A&A, 600, A129
```

```
Galazutdinov, G. A., Lee, J.-J., Han, I., et al. 2017, MNRAS, 467, 3099
García Pérez, A. E., Allende Prieto, C., Holtzman, J. A., et al. 2016, AJ, 151,
Geballe, T. R. 2016, J. Phys. Conf. Ser., 728, 062005
Geballe, T. R., Najarro, F., Figer, D. F., Schlegelmilch, B. W., & de La Fuente,
   D. 2011, Nature, 479, 200
Genoni, M., Riva, M., Pariani, G., Aliverti, M., & Moschetti, M. 2016, SPIE
   Conf. Ser., 9911, 99112L
Ghosh, S., Mondal, S., Das, R., & Khata, D. 2019, MNRAS, 484, 4619
Ghosh, S., Ojha, D. K., & Ninan, J. P. 2021, MNRAS, 501, 4596
Ghosh, S., Ninan, J. P., & Ojha, D. K. 2022, MNRAS, 511, 814
Gray, D. F. 2008, The Observation and Analysis of Stellar Photospheres (UK:
   Cambridge University Press)
Grevesse, N., Asplund, M., & Sauval, A. J. 2007, Space Sci. Rev., 130, 105
Guerço, R., Cunha, K., Smith, V. V., et al. 2019, ApJ, 885, 139
Gully-Santiago, M., Wang, W., Deen, C., & Jaffe, D. 2012, SPIE Conf. Ser.,
   8450, 84502S
Gustafsson, B., Edvardsson, B., Eriksson, K., et al. 2008, A&A, 486, 951
Hamano, S., Kobayashi, N., Kawakita, H., et al. 2022, ApJS, 262, 2
Han, J. Y., Yuk, I. S., Ko, K., et al. 2012, SPIE Conf. Ser., 8550, 85501B
He, B., Fan, D., Cui, C., et al. 2017, ASP Conf. Ser., 512, 153
Heiter, U., Jofré, P., Gustafsson, B., et al. 2015, A&A, 582, A49
Hinkle, K., Wallace, L., & Livingston, W. 1995, PASP, 107, 1042
Holtzman, J. A., Hasselquist, S., Shetrone, M., et al. 2018, AJ, 156, 125
Hunter, J. D. 2007, Comput. Sci. Eng., 9, 90
Jeong, U., Chun, M. Y., Oh, J. S., et al. 2014, SPIE Conf. Ser., 9154, 91541X
Jian, M., Matsunaga, N., & Fukue, K. 2019, MNRAS, 485, 1310
Jofré, P., Heiter, U., & Soubiran, C. 2019, ARA&A, 57, 571
Jönsson, H., Ryde, N., Harper, G. M., Richter, M. J., & Hinkle, K. H. 2014, ApJ,
   789, L41
Jönsson, H., Ryde, N., Nordlander, T., et al. 2017, A&A, 598, A100
Jönsson, H., Allende Prieto, C., Holtzman, J. A., et al. 2018, AJ, 156, 126
Jönsson, H., Holtzman, J. A., Allende Prieto, C., et al. 2020, AJ, 160, 120
Kupka, F. G., Ryabchikova, T. A., Piskunov, N. E., Stempels, H. C., & Weiss,
   W. W. 2000, Balt. Astron., 9, 590
Kurucz, R. L. 2007, Robert L. Kurucz on-line database of observed and predicted
   atomic transitions
Kurucz, R. L. 2014, Robert L. Kurucz on-line database of observed and predicted
   atomic transitions
Kurucz, R. L. 2016, Robert L. Kurucz on-line database of observed and predicted
   atomic transitions
Lawler, J. E., Guzman, A., Wood, M. P., Sneden, C., & Cowan, J. J. 2013, ApJS,
   205.11
Lebzelter, T., Hinkle, K. H., Straniero, O., et al. 2019, ApJ, 886, 117
Lee, J. J., Gullikson, K., & Kaplan, K. 2017, https://zenodo.org/record/
Li, G., Gordon, I. E., Rothman, L. S., et al. 2015, ApJS, 216, 15
Lind, K., Amarsi, A. M., Asplund, M., et al. 2017, MNRAS, 468, 4311
```

Mace, G., Sokal, K., Lee, J. J., et al. 2018, SPIE Conf. Ser., 10702, 107020Q

Maiolino, R., Haehnelt, M., Murphy, M. T., et al. 2013, ArXiv e-prints

Matsunaga, N., Jian, M., Taniguchi, D., & Elgueta, S. S. 2021, MNRAS, 506,

Fukue, K., Matsunaga, N., Yamamoto, R., et al. 2015, ApJ, 812, 64

Gaia Collaboration (Brown, A. G. A., et al.) 2021, A&A, 649, A1

```
Mawet, D., Fitzgerald, M., Konopacky, Q., et al. 2019, BAAS, 51, 134
Minchey, I., Steinmetz, M., Chiappini, C., et al. 2017, ApJ, 834, 27
Montelius, M., Forsberg, R., Ryde, N., et al. 2022, A&A, 665, A135
Moon, B., Wang, W., Park, C., et al. 2012, SPIE Conf. Ser., 8450, 845048
Mozurkewich, D., Armstrong, J. T., Hindsley, R. B., et al. 2003, AJ, 126, 2502
Nandakumar, G., Ryde, N., Montelius, M., et al. 2022, A&A, 668, A88
Nieuwmunster, N., Nandakumar, G., Spitoni, E., et al. 2023, A&A, 671, A94
Nissen, P. E., Hoeg, E., Schuster, W. J., et al. 1997, ESA Spec. Publ., 402, 225
Oh, J. S., Park, C., Cha, S. M., et al. 2014, SPIE Conf. Ser., 9147, 914739
Park, C., Jaffe, D. T., Yuk, I. S., et al. 2014, SPIE Conf. Ser., 9147, 91471D
Park, S., Lee, J.-E., Kang, W., et al. 2018, ApJS, 238, 29
Pinsonneault, M. H., Elsworth, Y. P., Tayar, J., et al. 2018, ApJS, 239, 32
Piskunov, N. E., Kupka, F., Ryabchikova, T. A., Weiss, W. W., & Jeffery, C. S.
   1995, A&AS, 112, 525
Ramírez, I., & Allende Prieto, C. 2011, ApJ, 743, 135
Randich, S., Gilmore, G., Magrini, L., et al. 2022, A&A, 666, A121
Recio-Blanco, A., de Laverny, P., Palicio, P. A., et al. 2023, A&A, 674, A29
Rich, R. M., Ryde, N., Thorsbro, B., et al. 2017, AJ, 154, 239
Richichi, A., Fabbroni, L., Ragland, S., & Scholz, M. 1999, A&A, 344, 511
Ryabchikova, T., Piskunov, N., Kurucz, R. L., et al. 2015, Phys. SCR, 90, 054005
Ryde, N., & Schultheis, M. 2015, A&A, 573, A14
Santos-Peral, P., Recio-Blanco, A., de Laverny, P., Fernández-Alvar, E., & Ordenovic, C. 2020, A&A, 639, A140
Sawczynec, E., Mace, G., Gully-Santiago, M., & Jaffe, D. 2022, AAS Meet.
   Abstr., 54, 203,06
Schlegel, D. J., Finkbeiner, D. P., & Davis, M. 1998, ApJ, 500, 525
Schultheis, M., Ryde, N., & Nandakumar, G. 2016, A&A, 590, A6
Sharma, K., Prugniel, P., & Singh, H. P. 2016, A&A, 585, A64
Skidmore, W., Bernstein, R., Dumas, C., et al. 2022, J. Astron. Telesc. Instrum.
   Syst., 8, 021510
Smith, V. V., & Lambert, D. L. 1990, ApJS, 72, 387
Smith, V. V., Cunha, K., Shetrone, M. D., et al. 2013, ApJ, 765, 16
Sneden, C., Lucatello, S., Ram, R. S., Brooke, J. S. A., & Bernath, P. 2014, ApJS,
   214, 26
Steinmetz, M., Matijevič, G., Enke, H., et al. 2020, AJ, 160, 82
Taniguchi, D., Matsunaga, N., Kobayashi, N., et al. 2018, MNRAS, 473,
Taniguchi, D., Matsunaga, N., Jian, M., et al. 2021, MNRAS, 502, 4210
Taylor, M. B. 2005, ASP Conf. Ser., 347, 29
Thorsbro, B., Ryde, N., Schultheis, M., et al. 2018, ApJ, 866, 52
Thorsbro, B., Ryde, N., Rich, R. M., et al. 2020, ApJ, 894, 26
Tody, D. 1993, ASP Conf. Ser., 173
Tsuji, T. 1981, A&A, 99, 48
Valenti, J. A., & Piskunov, N. 1996, A&AS, 118, 595
Valenti, J. A., & Piskunov, N. 2012, Astrophysics Source Code Library [record
   ascl:1202.013
van der Walt, S., Colbert, S. C., & Varoquaux, G. 2011, Comput. Sci. Eng., 13,
Virtanen, P., Gommers, R., Oliphant, T. E., et al. 2020, Nat. Methods, 17, 261
Wallace, L., & Livingston, W. 2003, An atlas of the solar spectrum in the
   infrared from 1850 to 9000 cm-1 (1.1 to 5.4 micrometer) (Tucson: National
   Solar Observatory, National Optical Astronomy Observatory, NSO Technical
Wang, W., Gully-Santiago, M., Deen, C., Mar, D. J., & Jaffe, D. T. 2010, SPIE
   Conf. Ser., 7739, 77394L
```

Yuk, I. S., Jaffe, D. T., Barnes, S., et al. 2010, SPIE Conf. Ser., 7735, 77351M

[arXiv:1310.3163]

Matteucci, F. 2021, A&ARv, 29, 5

1031

Appendix A: Additional tables

Table A.1. Line parameters of the Fe I lines.

Element	Wavelength	log (gf)	Broadening	α
	(Å)	0 .0 ,	by H ^a	
Fe	15485.454 ³	-0.828 3*	-7.290	
10	15490.881 ³	0.789^{3}	1618 1	0.325
	15500.799 ³	0.789^{3*}	1772 ¹	0.320
	15501.320 ³	0.789^{3*}	1620 ¹	0.325
	15502.174 ³	-1.034 ^{3*}	1876 ¹	0.317
	15662.013 ³	0.145^{3*}	1326 ²	0.235
	15878.444 ³	-0.339 ³ *	-7.450	
	16153.247 ³	-0.682 ^{3*}	924 ²	0.229
	16165.029 ³	0.782^{3*}	1598 ²	0.325
	16171.930 ³	-0.399 ³ *	1858 ²	0.373
	16174.975 ³	0.201^{3*}	1861 ¹	0.316
	16177.085 ³	-1.089 ³ *	-7.330	
	16179.583 ³	0.118^{3*}	1600^{-1}	0.325
	16180.900 ³	0.203^{3*}	1431^{-1}	0.329
	16182.170 ³	-0.805 ³ *	1599 ¹	0.325
	16185.799 ³	0.211^{3*}	1919 ¹	0.313
	16245.763 ³	-0.652 ³ *	1602^{-1}	0.325
	16246.458 ⁴	-0.106 ³ *	1419^{-1}	0.329
	16258.912 ³	-0.825 ^{3*}	-7.290	
	16316.320 ³	0.887^{3*}	1424^{-1}	0.329
	16318.690 ³	-0.436 ^{3*}	-7.550	
	16324.451 ³	-0.522 ³ *	936 ¹	0.229
	16331.524 ³	-0.506 ^{3*}	-7.470	
	16333.141 ³	-1.356 ^{3*}	-7.450	
	16517.223 ³	0.572^{3*}	1414^{-1}	0.329
	16612.761 ³	0.018^{3*}	1846 ¹	0.315
	16619.737 ³	-1.524 ³ *	1082^{-1}	0.228
	16783.037 ³	-0.695 ^{3*}	1409^{-1}	0.329
	16792.224 ³	-0.890 ^{3*}	1588 ¹	0.324
	16794.210 ³	-0.362 ³ *	-7.430	

Notes. a: Collisional broadening by neutral hydrogen gives either the broadening cross section $\sigma(v=10^4 \,\mathrm{m/s})$ in atomic units (a_0^2) , with the velocity parameter α (see text for more details), or, if the value is negative and no α is given, then the line width is given in the standard form $\log \Gamma/N_H$ at T=10000 K, where Γ is the full width at half maximum in rad/s and N_H is in cm⁻³. 1: BSYN based on routines from the MARCS code (Gustafsson et al. (2008)), 2: Paul Barklem (private communication), 3: Kurucz (2014), 4: Biemont et al. (1985), and the asterisk indicates an astrophysical estimate.

Table A.2. Line parameters of the lines of each element from which the abundances have been derived.

Element	Wavelength (Å)	log (gf)	Broadening by H ^a	α
Mg	21059.757 4*	-0.384 5*	4440 ³	1.10
C	21060.710 4*	-0.530 ⁵	4440^{3}	1.10
	21060.896 ⁴ *	-1.587 ⁵	4440^{3}	1.10
	21060.896 ⁴ *	-0.407 ⁵	4440^{3}	1.10
	21061.095 ⁴ *	-3.383 ⁵	4440 ³	1.10
	21061.095 ⁴ *	-1.583 ⁵	4440 ³	1.10
	21061.095 ⁴ *	-0.298 ⁵	4440 ³	1.10
	21458.962 ⁶	-1.319 ⁶	4840^{3}	0.359
Si	16434.933 ¹ *	-1.483 ¹ *	862 ³	0.288
	20804.225 1*	-1.026 ¹ *	861 ²	0.292
	20890.415 1*	-1.613 ¹ *	859 ²	0.292
	20926.149 ¹	-1.076 ¹ *	1484^{2}	0.324
Ca	16150.75 ^{1*}	-0.244 ¹ *	1872 ³	0.304
	16155.244 ^{1*}	-0.674 ¹ *	$1872^{\ 3}$	0.304
	16157.356 ^{1*}	-0.214 ¹ *	1946 ³	0.284
	20962.570 1*	-0.784 ¹ *	-7.230 ¹	
	20972.529 1	-1.002 ¹ *	-7.230 ¹	
Ti	16330.532 ⁷	-0.906 ⁷ *	484 ²	0.239
	21149.625 8*	0.789^{8*}	-7.440	

Notes. a: Collisional broadening by neutral hydrogen gives either the broadening cross section $\sigma(v=10^4 \text{m/s})$ in atomic units (a_0^2) , with the velocity parameter α (see text for more details), or, if the value is negative and no α given, then the line width is given in the standard form $\log \Gamma/N_H$ at T=10000 K, where Γ is the full width at half maximum in rad/s and N_H is in cm⁻³. 1: Kurucz (2007), 2: BSYN based on routines from the MARCS code (Gustafsson et al. (2008)), 3: Paul Barklem (private communication), 4: Brault & Noyes (1983), 5: Civiš et al. (2013), 6: manual entry by NIST lookup, 7: Lawler et al. (2013), 8: Kurucz (2016), and the asterisk indicates an astrophysical estimate.

Table A.3. Spectral line data of the OH molecular lines used in the method for determining stellar parameters. **Table A.4.** Spectral line data of the CN molecular lines used in the method for determining stellar parameters

Molecule	Wavelength	log (gf)	Molecule	Wavelength	log (gf)
	(Å)			(Å)	
OH	15236.623	-5.861	CN	15466.235	-1.195
	15236.956	-5.861		15471.812	-1.749
	15391.057	-5.512		15485.339	-1.779
	15391.205	-5.512		15489.56	-1.927
	15469.762	-5.242		15489.764	-1.932
	15470.216	-5.242		15494.748	-1.542
	15505.324	-5.378		15495.256	-1.196
	15505.746	-5.378		15496.319	-3.095
	15651.897	-5.203		15500.927	-1.742
	15653.480	-5.203		15501.498	-1.764
	15654.112	-6.808		15660.700	-1.521
	16247.884	-5.177		15661.595	-1.56
	16312.494	-5.077		15871.453	-1.633
	16312.920	-5.077		15881.108	-1.847
	16346.182	-5.002		16021.961	-1.518
	16347.493	-5.002		16179.943	-1.619
	16352.213	-4.897		16180.109	-1.131
	16581.269	-4.874		16329.245	-1.553
	16714.359	-4.758		16334.003	-1.932
	16872.277	-5.032		16352.092	-1.600
	16886.275	-4.874		16581.908	-1.215
	16886.293	-6.976		16582.026	-1.526
	16895.183	-4.743		16582.199	-1.109
	16895.319	-5.706		16615.321	-1.474
	16898.778	-4.743		16618.553	-1.891
	16902.733	-4.674		16791.783	-1.870
	16909.289	-4.712		16895.399	-1.462

Table A.5. Spectral line data of the CO molecular lines used in the method for determining stellar parameters

Molecule	Wavelength (Å)	log (gf)
	. ,	
CO	16025.53	-6.275
	16025.935	-7.004
	16026.94	-7.851
	16030.941	-6.262
	16031.274	-7.038
	16184.507	-6.26
	16184.565	-6.242
	16184.738	-6.279
	16184.912	-6.224
	16185.256	-6.298
	16185.548	-6.207
	16186.062	-6.317
	16186.473	-6.19
	16187.154	-6.337
	16187.688	-6.173
	16332.817	-5.79
	16334.087	-7.661
	16351.905	-7.148
	16352.478	-5.766
	16613.174	-5.777
	16613.225	-5.795
	16613.427	-5.759
	16613.579	-5.814
	16613.984	-5.742
	16614.236	-5.833
	16614.846	-5.724
	16615.195	-5.853
	16616.012	-5.708
	16616.457	-5.873
	16617.485	-5.691
	16618.021	-5.893
	16619.264	-5.675
	16619.887	-5.914
	16620.177	-7.028
	16871.668	-5.944
	16885.696	-6.849
	16895.397	-6.434
	16896.04	-5.293
	16899.304	-6.11
	16901.802	-6.527
	16902.455	-5.28
	16902.433	-5.266
	16909.543	-6.843

Table A.6. Magnesium abundances estimated from individual absorption lines, mean magnesium abundance and the standard error of mean estimated for each star.

Index / Star	21059.76 Å	21060.89 Å	21458.87 Å	<[Mg/Fe]>	σ [Mg/Fe] / $\sqrt{N_{lines}}$
1	-0.01	0.02	0.08	0.03	0.02
	0.03	0.06	0.09	0.06	0.01
2 3	0.21	0.14	0.26	0.21	0.02
4	0.07	0.02	0.08	0.06	0.01
5	-0.07	-0.04	-0.03	-0.05	0.01
6	-0.01	0.0	0.12	0.04	0.02
7	0.06	0.07	0.16	0.1	0.02
8	0.21	0.17	0.2	0.19	0.01
9	0.04	-0.01	0.07	0.04	0.02
10	0.26	0.3	0.34	0.3	0.02
11	0.01	-0.01	0.08	0.03	0.02
12	0.05	-0.0	0.1	0.05	0.02
13	-0.16	-0.08	-0.06	-0.1	0.02
14	0.07	0.05	0.14	0.09	0.02
15	-0.14	-0.12	-0.02	-0.09	0.02
16	-0.18	-0.11	-0.09	-0.13	0.02
17	0.04	0.09	0.18	0.1	0.03
18	-0.07	0.07	0.12	0.04	0.03
19	-0.06	-0.03	0.01	-0.03	0.01
20	-0.03	-0.01	0.06	0.0	0.02
21	-0.15	-0.09	-0.06	-0.1	0.02
22	-0.12	-0.01	-0.04	-0.05	0.02
23	0.08	-0.1	0.02	-0.0	0.03
24	-0.05	-0.11	-0.05	-0.07	0.01
25	-0.16	-0.2	-0.12	-0.16	0.02
26	-0.13	-0.07	-0.02	-0.08	0.02
27	-0.12	-0.1	-0.07	-0.09	0.01
28	-0.08	-0.11	-0.02	-0.07	0.02
29	0.03	0.09	0.13	0.08	0.02
30	-0.07	-0.06	0.0	-0.04	0.02
31	-0.27	-0.15	-0.11	-0.18	0.03
32	-0.12	-0.14	-0.07	-0.11	0.01
33	-0.12	-0.12	-0.06	-0.1	0.01
34	-0.01	0.0	0.03	0.01	0.01
35	-0.02	0.01	0.03	0.01	0.01
36	-0.11	-0.1	-0.05	-0.09	0.01
37	-0.12	-0.09	-0.07	-0.09	0.01
38	-0.18	-0.13	-0.06	-0.12	0.02
39	0.21	0.28	0.25	0.25	0.01
40	-0.2	-0.13	-0.14	-0.16	0.01
41	-0.18	-0.18	-0.03	-0.13	0.03
42	-0.07	-0.07	0.01	-0.04	0.02
43	-0.14	-0.12	-0.05	-0.1	0.02
44	0.2	0.19	0.3	0.23	0.02
HD132813	-0.04	-0.09	0.06	-0.03	0.03
HD175588	-0.18	-0.19	-0.01	-0.03	0.03
HD89758	-0.1	-0.13	-0.01	-0.13	0.03
HD224935	-0.12	-0.13	0.06	-0.05	0.03
HD101153	-0.12	-0.09	0.00	-0.04	0.03
HIP54396	-0.06	-0.02	0.09	0.0	0.04
1111 34370	-0.00	-0.02	0.00	0.0	0.03

Table A.7. Silicon abundances estimated from individual absorption lines, mean silicon abundance and the standard error of mean estimated for each star.

Index / Star	16434.93 Å	20804.20 Å	20890.37 Å	20926.14 Å	<[Si/Fe]>	σ [Si/Fe] / $\sqrt{N_{lines}}$
1	0.21	0.04	0.08	0.02	0.09	0.03
2	0.06	0.05	0.1	0.06	0.07	0.0
3	0.37	0.28	0.17	0.2	0.26	0.04
4	0.18	_	_	_	0.18	0.0
5	0.06	0.06	0.09	-0.17	0.01	0.04
6	0.15	0.04	0.02	-0.0	0.05	0.02
7	0.11	_	0.06	_	0.08	0.01
8	0.26	0.34	0.06	0.34	0.25	0.04
9	0.1	0.13	0.13	0.06	0.1	0.02
10	0.38	0.29	0.36	0.36	0.35	0.01
11	0.1	0.03	-0.01	0.24	0.09	0.04
12	0.03	0.13	0.07	0.0	0.06	0.02
13	0.04	-0.07	0.05	0.0	0.01	0.02
14	0.17	0.13	0.15	-0.01	0.11	0.02
15	0.07	0.07	_	-0.13	0.0	0.04
16	0.01	-0.06	-0.0	-0.15	-0.05	0.03
17	0.22	_	0.02	_	0.12	0.05
18	0.15	0.1	_	_	0.12	0.01
19	-0.0	0.02	-0.12	-0.07	-0.04	0.02
20	-0.03	-0.02	0.13	-0.08	-0.0	0.03
21	-0.08	0.0	-0.02	-0.07	-0.04	0.02
22	-0.01	-0.08	-0.11	-0.13	-0.08	0.02
23	-0.04	-0.18	-0.08	0.22	-0.02	0.06
24	-0.14	-0.01	_	-0.06	-0.07	0.02
25	-0.08	-0.02	-0.22	-0.04	-0.09	0.03
26	-0.16	0.08	_	0.05	-0.01	0.05
27	-0.13	-0.01	-0.09	-0.0	-0.06	0.02
28	0.02	-0.05	_	-0.11	-0.05	0.02
29	0.12	0.07	0.02	0.07	0.07	0.02
30	0.01	0.04	-0.05	0.02	0.01	0.01
31	-0.06	-0.08	0.06	-0.11	-0.05	0.02
32	-0.03	0.0	-0.08	0.01	-0.02	0.02
33	-0.08	0.12	-0.12	0.08	0.0	0.05
34	-0.16	0.01	-0.0	-0.03	-0.05	0.02
35	0.04	0.03	0.0	0.0	0.02	0.0
36	0.04	-0.0	0.01	-0.02	0.01	0.01
37	0.04	0.01	0.04	-0.16	-0.02	0.03
38	-0.18	-0.03	_	-0.02	-0.08	0.03
39	0.19	0.05	0.12	0.18	0.13	0.02
40	0.04	0.06	-0.06	0.04	0.02	0.02
41	-0.14	-0.03	-0.14	-0.03	-0.09	0.03
42	-0.0	0.11	-0.01	0.01	0.03	0.02
43	-0.13	0.0	-0.11	-0.09	-0.08	0.02
44	0.45	0.24	0.34	0.28	0.33	0.04
HD132813	-0.05	0.07	_	_	0.01	0.03
HD175588	-0.09	-0.0	0.12	-0.07	-0.01	0.04
HD89758	0.1	0.01	-0.04	-0.01	0.02	0.02
HD224935	-0.05	-0.11	0.01	0.06	-0.02	0.03
HD101153	-0.02	-0.02	0.04	0.01	0.0	0.01
HIP54396	-0.14	0.03	0.09	_	-0.01	0.05

Table A.8. Calcium abundances estimated from individual absorption lines, mean calcium abundance and the standard error of mean estimated for each star.

Index / Star	16136.82 Å	16150.76 Å	16155.24 Å	16157.36 Å	20962.57 Å	20972.53 Å	<[Ca/Fe]>	σ [Ca/Fe] / $\sqrt{N_{lines}}$
1	-0.03	-0.01	0.09	0.01	0.07	0.09	0.04	0.02
2	-0.02	0.05	0.07	0.08	0.05	0.07	0.05	0.01
3	0.14	0.14	0.18	0.11	0.16	0.19	0.15	0.01
4	-0.13	-0.0	-0.02	-0.04	0.01	-0.08	-0.04	0.02
5	-0.22	-0.18	0.0	-0.13	-0.01	-0.08	-0.1	0.04
6	-0.07	0.01	0.04	-0.0	0.06	0.04	0.01	0.01
7	0.09	0.06	0.13	0.01	0.17	0.21	0.11	0.02
8	0.02	0.05	0.14	0.04	0.22	0.17	0.11	0.03
9	0.02	-0.04	0.1	-0.02	0.1	0.07	0.04	0.02
10	0.26	0.22	0.24	0.19	0.21	0.32	0.24	0.01
11	0.01	0.04	0.08	0.01	0.03	0.13	0.05	0.02
12	0.02	0.06	0.09	0.01	0.09	0.07	0.06	0.02
13	-0.05	-0.01	0.07	-0.01	0.08	0.09	0.03	0.02
14	0.01	0.0	0.1	0.02	0.11	0.11	0.06	0.02
15	-0.04	-0.0	0.09	0.01	0.09	0.08	0.04	0.02
16	-0.23	-0.18	-0.11	-0.17	-0.06	-0.09	-0.14	0.02
17	0.05	-0.13	0.04	0.04	0.13	0.03	0.04	0.02
18	-0.05	-0.03	0.04	-0.0	0.13	0.05	0.04	0.01
19	-0.03	-0.01	0.03	-0.03	-0.0	0.05	-0.03	0.03
20	-0.14	-0.09	0.04	0.02	0.12	0.1	0.03	0.03
21	-0.06	-0.01	0.12	-0.02	0.12	0.11	0.04	0.03
22	-0.06	-0.02	0.12	-0.02	0.11	0.11	-0.02	0.03
23	-0.13	0.13	0.04	0.0	0.07	0.08	0.02	0.04
24	-0.1	-0.06	0.02	-0.04	-0.02	0.02	-0.02	0.01
	-0.07	0.04	0.03	-0.04	0.02	0.03	0.02	0.02
25 26								
26 27	-0.08 -0.11	-0.05 -0.04	0.01 0.04	-0.01 -0.07	0.06 0.05	0.07 0.02	0.0 -0.02	0.02 0.02
28 29	-0.09 -0.21	-0.02 -0.17	0.04 -0.02	-0.05 -0.08	0.07 0.01	0.13 -0.0	0.01 -0.08	0.03 0.04
30	-0.21	-0.17	0.05	-0.08	0.01	0.12	0.01	0.04
31	-0.18	-0.11	-0.0	-0.14	0.02	0.04	-0.06	0.04
32	-0.1	-0.06	0.03	-0.05	0.03	0.05	-0.02	0.02
33	-0.12	-0.01	0.07	-0.05	0.02	0.05	-0.01	0.02
34	-0.07	-0.0	0.12	0.02	0.11	0.15	0.06	0.03
35	-0.09	-0.04	0.08	-0.01	0.08	0.11	0.02	0.03
36	-0.01	0.0	0.12	-0.03	0.06	0.16	0.05	0.03
37	-0.16	-0.12	0.0	-0.09	0.0	0.01	-0.06	0.03
38	-0.16	-0.12	-0.06	-0.12	0.03	0.03	-0.07	0.03
39	0.12	0.07	0.19	0.14	0.24	0.17	0.16	0.02
40	-0.13	-0.12	0.02	-0.15	0.01	0.09	-0.05	0.03
41	-0.04	0.05	0.17	0.02	0.08	0.14	0.07	0.03
42	0.01	0.02	0.12	-0.0	0.05	0.12	0.05	0.02
43	-0.04	-0.0	0.1	-0.01	0.07	0.1	0.04	0.02
44	0.21	0.16	0.24	0.14	0.26	0.27	0.21	0.02
HD132813	-0.03	-0.02	0.02	-0.1	0.12	0.19	0.03	0.04
HD175588	-0.06	-0.03	0.07	-0.1	0.13	0.18	0.03	0.04
HD89758	-0.1	-0.08	0.06	-0.06	0.09	0.04	-0.01	0.03
HD224935	-0.11	-0.07	0.04	-0.1	_	0.12	-0.02	0.04
HD101153	-0.14	-0.06	0.02	-0.15	_	0.13	-0.04	0.04
HIP54396	-0.11	-0.05	0.03	-0.09	0.13	0.13	0.01	0.04

Table A.9. Titanium abundances estimated from individual absorption lines, mean titanium abundance and the standard error of mean estimated for each star.

Index / Star	16330.54 Å	21149.62 Å	<[Ti/Fe]>	σ [Ti/Fe] / $\sqrt{N_{lines}}$
1	0.08	0.11	0.1	0.01
2	0.01	0.32	0.17	0.07
2 3	0.2	0.31	0.25	0.03
4	0.04	0.04	0.04	0.0
5	-0.08	0.07	-0.01	0.04
6	0.07	_	0.07	0.0
7	0.13	0.31	0.22	0.04
8	0.22	0.38	0.3	0.04
9	0.09	-0.03	0.03	0.03
10	0.36	0.43	0.39	0.01
11	0.1	0.21	0.16	0.03
12	0.08	0.2	0.14	0.03
13	0.02	0.23	0.12	0.05
14	0.12	0.34	0.23	0.05
15	-0.03	0.23	0.1	0.06
16	-0.1	0.01	-0.04	0.03
17	0.04	0.06	0.05	0.01
18	0.08	0.08	0.08	0.0
19	0.01	0.01	0.01	0.0
20	0.0	0.03	0.02	0.01
21	0.0	0.02	0.01	0.01
22	-0.09	0.1	0.01	0.04
23	-0.04	-0.05	-0.05	0.0
24	-0.05	0.08	0.01	0.03
25	-0.0	0.11	0.05	0.03
26	0.12	-0.03	0.04	0.04
27	-0.0	0.09	0.04	0.02
28	-0.01	0.08	0.03	0.02
29	-0.06	0.12	0.03	0.04
30	0.01	0.05	0.03	0.01
31	-0.12	-0.03	-0.08	0.02
32	0.02	0.02	0.02	0.0
33	-0.01	0.06	0.02	0.01
34	0.01	0.0	0.0	0.0
35	0.04	0.09	0.07	0.01
36	0.02	0.08	0.05	0.01
37	-0.08	0.03	-0.02	0.03
38	-0.06	-0.02	-0.04	0.01
39	0.14	0.26	0.2	0.03
40	-0.11	0.01	-0.05	0.03
41	-0.02	0.12	0.05	0.04
42	-0.02	0.04	0.01	0.01
43	-0.02	0.04	0.01	0.01
44	0.28	0.03	0.32	0.01
HD132813	0.28	0.37	0.32	0.02
HD175588	-0.05	0.24	0.12	0.06
HD89758	-0.03	0.2	0.07	0.06
HD224935	-0.07	0.2	0.00	0.06
HD101153	-0.01	0.26	0.12	0.06
HIP54396	-0.08	0.10	0.04	0.03
ПІГ 34390	-0.02	0.12	0.03	0.03

Table A.10. Uncertainties in the derived Mg, Si, Ca, and Ti abundances from each individual line arising from typical uncertainties of \pm 100 K in $T_{\rm eff}$, \pm 0.2 dex in $\log g$, \pm 0.1 dex in [Fe/H], and \pm 0.1 km/s in $\xi_{\rm micro}$. We selected seven stars with metallicities covering the range explored in this study (metallicities are mentioned in brackets below the name of each star). The abundance uncertainty, i.e., the dispersion estimated from the Gaussian fit to the distribution of 50 abundance estimates (estimated using 50 sets of stellar parameters) from each line is listed in each column. The mean uncertainty based on the error propagation is listed in the row after each element.

	Index	10	44	11	30	29	41	40
	[Fe/H]	-0.9 dex	-0.6 dex	-0.5 dex	-0.25 dex	$0.0 \mathrm{dex}$	0.1 dex	0.25 dex
	λ(Å)	σ_{line}	σ_{line}	σ_{line}	σ_{line}	σ_{line}	σ_{line}	σ_{line}
[Mg/Fe]	21059.76	0.10	0.08	0.10	0.08	0.09	0.11	0.12
	21060.89	0.12	0.12	0.14	0.07	0.13	0.13	0.13
	21458.87	0.10	0.10	0.10	0.10	0.11	0.12	0.14
$\sqrt{\sum_{\sigma_{line}^2}} / N_{lines}$		0.04	0.04	0.07	0.05	0.07	0.07	0.08
[Si/Fe]	16434.93	0.2	0.33	0.28	0.27	0.34	0.30	0.36
	20804.20	0.13	0.12	0.14	0.15	0.15	0.15	0.13
	20890.37	0.11	0.07	0.12	0.10	0.13	0.11	0.13
	20926.14	0.13	0.10	0.14	0.15	0.16	0.11	0.17
$\sqrt{\sum_{\sigma_{line}^2}}$ / N_{lines}		0.07	0.09	0.09	0.09	0.11	0.09	0.11
[Ca/Fe]	16150.76	0.14	0.18	0.12	0.21	0.16	0.25	0.09
	16155.24	0.10	0.10	0.08	0.14	0.12	0.13	0.06
	16157.36	0.14	0.10	0.09	0.14	0.10	0.13	0.12
	20962.57	0.09	0.08	0.07	0.11	0.08	0.10	0.10
	20972.53	0.12	0.06	0.10	0.12	0.11	0.09	0.09
$\sqrt{\sum_{\sigma_{line}^2}}$ / N_{lines}		0.05	0.05	0.04	0.07	0.05	0.07	0.05
[Ti/Fe]	16330.54	0.14	0.14	0.09	0.19	0.14	0.20	0.08
	21149.62	0.17	0.15	0.11	0.12	0.09	0.09	0.10
$\sqrt{\sum_{\sigma_{line}^2}}$ / N_{lines}		0.11	0.10	0.07	0.11	0.08	0.11	0.06